Performance Evaluation of State-of-the-Art High-Resolution Time-of-Flight Cameras

Alvaro Lopez Paredes, *Graduate Student Member, IEEE*, Qiang Song, *Graduate Student Member, IEEE*, and Miguel Heredia Conde, *Member, IEEE*

***Abstract*—It has been about 20 years since the disruptive appearance of the first time-of-flight (ToF) cameras. Since then, ToF imaging has progressively evolved. Nowadays, ToF sensors have broken the barrier of the 1-megapixel resolution, and a significant number of high-resolution ToF cameras have appeared in the market. To provide a better understanding of their performance and applications, we experimentally evaluate three state-of-the-art high-resolution ToF cameras such as Azure Kinect, Helios2, and S100D, together with the solid-state LiDAR L515. We perform various experiments to examine some key parameters, such as warm-up times, accuracy, precision, lateral and axial resolutions, edge noise, unsteady scenes, and modulated waveform and optical power. Our evaluation draws various conclusions: S100D shows fluctuations within 1 mm after being powered up while the others require warm-up times. Azure Kinect, Helios2, and L515 can achieve precision within 2 mm in a measuring range of 0.5–3 m. Helios2 and S100D are more severely affected by dynamic scenes. Finally, the point clouds (PCs) generated for a white panel at a distance of 1.5 m show that flying pixels are present in all cameras, being this problem less acute for the L515.**

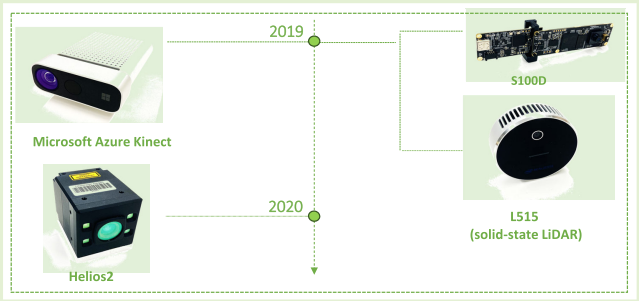

***Index Terms*— 3-D imaging, depth imaging, high-resolution, metrological validation, time-of-flight (ToF).**

I. Introduction

THE rapid development of the technology over the past few decades have allowed tackling challenges which seemed unsolvable just some years ago. Nowadays, computer vision systems are capable of, without human intervention, perceiving and reconstructing the surrounding reality and reliably making decisions based on the predicted behavior of the targets this reality consists of. The continuous advancements on computer vision, together with the increase in computational capabilities and the development of more efficient reconstruction techniques, have facilitated a better representation of the surrounding environment, allowing access to previously unreachable locations and a safer development of tasks which can now be performed remotely. There are some fields, such as autonomous driving or mobile robotics, in which this impact has become more evident. In them, the need for reliable, high-resolution, high-frame-rate 3cD imaging is of paramount importance. This article is focused on the study of 3-D imaging technologies and, in particular, on the empirical evaluation of various state-of-the art time-of-flight (ToF) cameras. A ToF camera features an active illumination system and retrieves the distance by measuring the round trip of a light signal between the sensor and the target. Due to the relatively low cost and power consumption, they will play a relevant role in the market in coming years. Also, they do not present problems such as the correspondence of points from multiple views of stereovision [1] or the sensitivity of structured light to external illumination [2].

The revolutionary research of Prof. Rudolf Schwarte in the 1990s at the Center for Sensor Systems (ZESS) of the University of Siegen (Germany) yielded the birth of the first ToF camera in 2001 [3] based on the photonic mixer device (PMD) technology. Since then, significant efforts have been invested to enhance the resolution, increase the range, reduce the computational needs, and allow for the use in demanding environments, i.e., under strong light conditions or unsteady scenarios. As a result, a large number of ToF cameras have

Manuscript received 31 March 2023; accepted 30 April 2023. Date of publication 9 May 2023; date of current version 14 June 2023. This work was supported by the European Union's Horizon 2020 Research and Innovation Programme under the Marie Skłodowska-Curie Grant 860370 (MENELAOS-NT). The associate editor coordinating the review of this article and approving it for publication was Dr. Brajesh Kumar Kaushik. *(Corresponding author: Alvaro Lopez Paredes.)*

Alvaro Lopez Paredes and Qiang Song are with the Center for Sensor Systems (ZESS), University of Siegen, 57076 Siegen, Germany (e-mail: alvaro.lparedes@uni-siegen.de; songqiang5253@gmail.com).

Miguel Heredia Conde is with the Center for Sensor Systems (ZESS), University of Siegen, 57076 Siegen, Germany, and and also with the Centro Singular de Investigación en Tecnoloxías Intelixentes (CiTIUS), University of Santiago de Compostela, 15782 Santiago de Compostela, Spain. (e-mail: heredia@zess.uni-siegen.de).

Digital Object Identifier 10.1109/JSEN.2023.3273165

been introduced in the market. In this article, we compare the performance of three recently launched high-resolution phase shift ToF cameras, such as Microsoft Azure Kinect (2019), S100D (2019), and Helios2 (2020), together with a LiDAR, L515 (2019). We perform an experimental evaluation under controlled environmental conditions in a dedicated facility [4] and present results which will allow for a better understanding of their performance, strengths, and limitations.

The rest of this article is structured as follows. Section II presents an overview of relevant works in the field. In Section III, the historical evolution of 3-D imaging technologies and, in particular, ToF imaging systems is depicted, together with a detailed description of the cameras evaluated, the key operational parameters, and the main sources of errors. In Section IV, we describe the experimental setup and present the results obtained. Finally, in Section V, we summarize the main outcomes of our work and identify areas for future research.

II. Related Work

Since the birth of ToF imaging systems, many significant efforts have been made to examine the operational parameters of ToF cameras and the nature of the main measurement errors and inaccuracies to compensate them and guarantee acceptable depth results. Kahlman et al. [5] investigated a sensor calibration procedure for the range imaging camera Swissranger[1] adopting a parameter-based approach, modeling the evolution of the measured distance during the warm-up, compensating the depth errors per pixel by making use of a fixed pattern noise (FPN) matrix, and mitigating wiggling errors using a lookup table (LUT). In the same year, Lindner and Kolb [6] proposed an accurate distance-calibration procedure, based on B-spline curve-fitting, which significantly reduced the amount of data stored per pixel. May et al. [7] proposed a technique for the removal of edge noise by a filtering approach. Foix et al. [8] extensively reviewed the state-of-the-art of ToF imaging, presenting the main sources of errors and calibration techniques. Hussman et al. [9] generated better modulated optical signals through hardware, although the range of application was substantially limited by the optical power. Feigin et al. [10] proposed the modeling of circular errors as a multipath interference (MPI) problem which could be solved by making use of multiple modulation frequencies and avoided via prior calibration. An interesting work was performed by Georgiev et al. [11], who discussed the modeling and removal of FPN in low-light conditions, i.e., scenes characterized by poor illumination conditions, or low-reflectivity targets. The study and compensation of FPN in ToF systems was also the object of recent research in [12]. He et al. [13] analyzed the impact of external factors on the depth errors of ToF cameras by performing an experimental evaluation using a MESA SR-4000 and proposed an error correction method based on particle filter-support vector machine (PF-SVM) which reduced the depth error to the millimeter range over the whole measurement range.

In addition, various works have evaluated the performance of low- and medium-resolution ToF cameras on the experimental front. Piatti and Rinaudo [14] empirically compared the performance of the MESA SR-4000 and PMDTec CamCube 3.0. They found that both the cameras required warm-up times of, at least, 40 min, and that the measurement precision reached a standard deviation $\sigma \sim \mathcal{O}(\text{mm})$ and significantly depended on the integration time. Laukannen [15] tested the MESA SR-4000, Panasonic D-IMager EKL-3106, and Microsoft Kinect V2 and showed that D-IMager EKL-3106 required much shorter times $\approx$ 15 min to reach steady-state conditions. The PMDTec Camboard Picoflexx and Microsoft Kinect v2 were compared in the context of motion capture for human body kinematics measurement [16], where a better performance of the latter was observed, although both could satisfactorily operate in such context. Fürsattel et al. [17] performed an extensive comparative error analysis of eight cameras launched between 2005 and 2013. Langmann et al. [18] evaluated the lateral and depth resolution of the PMDTec 3k-S, Microsoft Kinect V1, and PMDTec CamCube 41k for near-field indoor scenes. Over the past few years, the Microsoft Azure Kinect and her precursor models Kinect V1 and V2 have attracted attention within our community [19], [20], [21] and have been applied to many fields such as human detection and tracking [22], [23] or posture recognition [24], among others. Recently, Wei et al. [25] performed a thorough comparison of the three generations of the Kinect family and recommended some operational parameters for different scenarios. Lourenço and Araujo [26] compared various 3-D

[1]Trademarked.

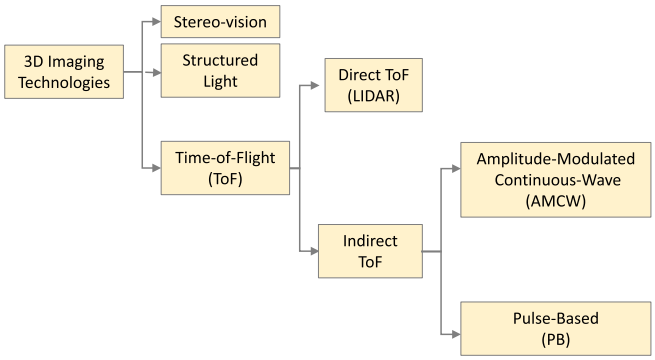

Fig. 1. 3-D imaging technologies.

TABLE I
Comparison of 3-D Imaging Technologies

Parameter	ToF	Stereo-vision	Structured light
Active illumination	Yes	No	Yes
Software complexity	Low	High	Medium
MPI	Yes	No	Yes
Low-light performance	Good	Weak	Good
Outdoor performance	Medium	Good	Weak
Latency	Low	Medium	Medium
Range	Long	Medium	Short
Depth Resolution	Medium	Medium	High
Power consumption for camera	Medium	Medium	Medium
Power consumption for processing	Low	High	High
Alignment	No	Yes	Yes
Size	small	baseline-lim.	baseline-lim.

TABLE II
SPECIFICATIONS OF ToF CAMERAS

Parameter	Azure Kinect	Helios2	S100D	L515
Release date	2019	2020	2019	2019
Supplier	Microsoft	LUCID Vision Labs	Meerecompany CubeEye	Intel
Sensor Model	Microsoft	Sony IMX556PLR	Samsung ISOCELL Vizion 3D	Intel
Dimensions [mm]	$103 \times 39 \times 126$	$60 \times 60 \times 77.5$	$60 \times 15 \times 69$	61×26
Working principle	AMCW-ToF	AMCW-ToF	AMCW-ToF	LiDAR
Number of emitters	2	4	1	1
Emitter	-	VCSEL $\lambda = 850$ nm	VCSEL $\lambda = 940$ nm	IR Laser $\lambda = 860$ nm
Pixel size [μm]	3.5×3.5	10×10	7×7	-
Min range [m]	0.25	0.3	0.2	0.25
Max range [m]	5.46	8.33	4	9
Horizontal FOV [°]	90	69	60	70
vertical FOV [°]	74.3	51	45	55
Max. resolution [pix]	1024×1024	640×480	640×480	1024×768
Max. frame rate [fps]	30	30	30	30
Min. op. temperature [degC]	10	-10	-15	0
Max. op. temperature [degC]	25	60	50	30
Power consumption [W]	< 5.9	< 12	1.5	< 3.5
Weight [g]	440	398	4.9	95
RGB camera	Yes	No	No	Yes
IMU	Yes	No	No	Yes
Estimated price [$]	399	1495	535	349

cameras from Intel[2] RealSense[1] based on different working principles, such as the SR305 (structured light), D415 (stereovision), and L515 (direct-ToF), and showed that the latter presented a better performance in terms of accuracy (lowest number of failed points). This was confirmed by Servi et al. [27], who performed a metrological characterization and comparison of three depth cameras, namely, D415, D455, and L515, in the close range, i.e., from 0.1 to 1.5 m. They showed that the L515 presented smaller systematic depth errors, although the D415 attained a better reconstruction quality in the short-range test (0.1–0.5 m) and the D455 in the standard-range test (0.5–1.5 m). A comparison of ToF and other imaging technologies such as structured light and active stereoscopy was presented in [28]. They extensively described various state-of-the-art imaging devices and performed a metrological validation of the Microsoft Kinect V2. They verified the modulated signal, evaluated the stability and response to temperature fluctuations, and analyzed the range measurement at a single-pixel and sensor level. Also, Frangez et al. [29] experimentally evaluated the deviations of the depth measurements for two phase-shift-based cameras of the same model (Lucid Helios). They obtained results very close to ours (see Figs. 7 and 8 in Section IV), such as required warm-up times of ≈40 min to reach a depth error ≤ 2.5 mm and standard deviation $\sigma \leq 3$ mm for up to a range $r \approx 2$ m.

III. THEORETICAL BACKGROUND

A. ToF and Other 3-D Imaging Technologies

The ToF imaging systems estimate the relative distance between the camera and the surrounding objects, i.e., targets the scene under study consists of, by calculating the return-trip time of a light signal from the camera to them. As shown in Fig. 1, there are two fundamental approaches for ToF imaging, depending on whether the time delay is directly measured, as in LiDARs based on single-photon avalanche diodes (SPADs) [30], or whether it is calculated by performing a correlation of the reflected signal and a set of reference control signals generated in the camera. In indirect-ToF, the nature of the used signals leads to a further distinction between amplitude-modulated continuous-wave (AMCW) and pulse-based (PB) ToF systems. In AMCW-ToF, the emitted and reference control signals are sinusoidal, or, in practice, smoothed trapezoidal signals due to the implementation of digital logic. In PB-ToF cameras [31], [32], [33], only a short light pulse is emitted, interacts with the scene, and is captured by one or more pixels of the sensor array in a very short time window or gate. The pixel is equipped with two optical shutters, which generate two control signals with the same period as the emitted pulse signal. Then, the distance is calculated from the correlation of both, the reflected and control, signals. Moreover, there are other popular 3-D imaging technologies, such as stereovision and structured light, to provide depth information which make use of different working principles. In **stereovision** systems [34], a 3-D representation of the surrounding space is generated by considering different perspectives from several cameras or from a moving camera. In **structured light** systems [2], one of the cameras is replaced by a projector. The projector emits an illumination pattern distorted by the nonplanar scene, and the depth is estimated from the distortion with respect to the original, which is acquired by a conventional image sensor. Table I presents a comparison of ToF with respect to stereovision and structured light. It can be seen that ToF cameras represent a cost-effective, low-power, and size-manageable solution for long ranges, which, moreover, can work indoors and outdoors with medium to high resolution [$\sim\mathcal{O}$(cm)].

B. Historical Evolution of ToF Cameras

In this section, we present some of the most remarkable milestones in the historical development of ToF cameras since the appearance of the first PMD ToF prototype in 1999 [35].

[2]Registered trademark.

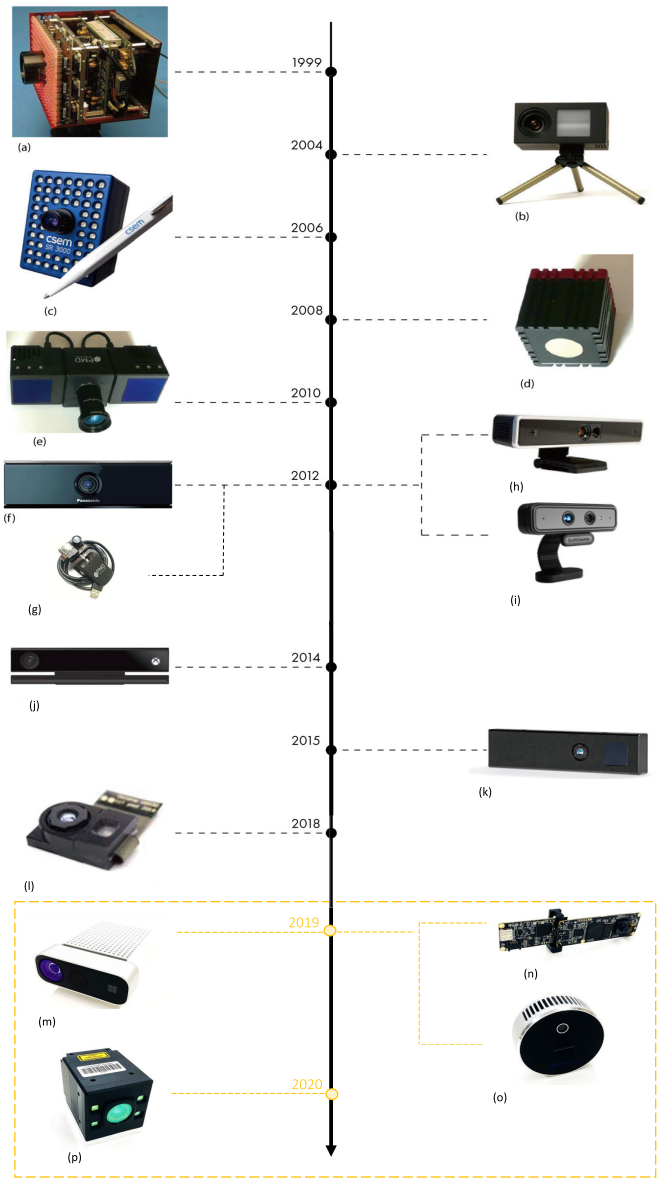

Fig. 2. Historical evolution of ToF cameras. (a) PMD first ToF prototype. (b) Canesta DP 200. (c) MESA SR3000. (d) MESA SR4000. (e) PMD Camcube3.0. (f) Panasonic D-IMager EKL3106. (g) PMD Camboard Nano. (h) Softkinect DS311. (i) Softkinect DS325. (j) Microsoft Kinect V2. (k) PMD Camboard Picoflexx. (l) PMD Selene Module. (m) Microsoft Azure Kinect. (n) S100D. (o) L515 (solid-state LiDAR). (p) Helios2.

Fig. 2 presents some of the most popular ToF cameras [14], [36], [37], [38], [39] developed over the past two decades.

PMD Technologies, a spin-off of the Center for Sensor Systems (ZESS) at the University of Siegen (Germany), was founded in 2002 after their core technology, the Photo-Mixer Device. Their founders Schwarte [39] and the Audi Electronics Venture GmbH pioneered the ToF imaging technology. Their first release was the PMDTec 3k-S. In 2010, the company launched a CW-ToF camera with a significant improvement on the performance, the Camcube 3.0. This camera featured a 200 × 200 pixel array and achieved a range of 7.5 m. In 2012, PMD released the PMD Camboard Nano and, in 2015, the PMD Camboard Picoflexx. The manageable size and low weight of the camera allowed for the integration on mobile devices. Since 2013, PMD and Infineon have jointly developed and launched in the market six generations of the state-of-the-art ToF imagers [40]. In 2018, PMD launched an small-size module, the Selene Module, which has been used in some researches for material identification [41] and evaluation and compensation of the effect of dirt [42].

Canesta [43] launched the first ToF camera DP200 in 2004, which featured a maximum field of view (FOV) of 70° × 70° and a frame rate of 30 frames/s. Over the following years, the camera was implemented in several fields [44], [45]. The company was acquired by Microsoft in 2010. In the same year, Microsoft released the Microsoft Kinect for the XBOX 360, used in video games for 3-D perception, i.e., gesture recognition and body skeleton detection. The low cost and high performance brought the attention of scientists and robotics enthusiasts [46], who expanded the range of applications to object recognition and simultaneous localization and mapping (SLAM) [47], [48]. Microsoft released Kinect V1 in 2012 and V2 in 2014, respectively, for commercial use. Kinect V1 was based on the structured light technology of PrimeSense, while Kinect V2 was a phase-shifted ToF camera. The Kinect V2 marked an important milestone on ToF technology because of its high depth resolution sensor array of 512 × 424 pixel. The latest release of Microsoft is the Azure Kinect [49] based on AMCW-ToF. The camera features a sensor of 1024 × 1024 pixel and a bandwidth up to 320 MHz. The camera was presented at the Mobile World Congress (MWC) in Barcelona in 2019 and released to the general public in 2020.

The research group lead by Peter Seitz at the Centre Suisse d'Electronique et Microtechnique (CSEM) was also one of the precursors on the development of ToF cameras [50]. The group provided the technical development for the foundation of MESA Imaging AG, a spin-off company of the CSEM founded in 2006. Mesa Imaging released two AMCW ToF cameras, SR-3000 [51] and SR-4000 [52], in 2006 and 2008, respectively [53]. SR-4000 presented two main improvements with respect to the previous model, such as the internal reference path, which realizes internal synchronization between the illumination and the sensor, and a more stable passive cooling system [53]. The SR-4000 featured an image sensor of 176 × 144 pixel and two different modes with measurement ranges of $5-10$ m, respectively. In 2014, Mesa Imaging was bought by Heptagon, later acquired by AMS AG in 2017.

Softkinect launched two ToF cameras in 2012, DS311 and DS325 [37]. Comparatively, the DS311 presented a larger measurement range up to 5 m, and the DS325 had a higher resolution with a sensor array of 320 × 240 pixel and FOV of 74° × 58°. In 2015, Sony announced the acquisition of Softkinect. In 2016, they developed a small ToF camera [54], the DS541, suitable for integration in mobile devices. Their latest ToF sensor, which achieves video graphics array (VGA) resolution, is the IMX556PLR, which is featured by the Lucid Helios2 [55].

C. Description of Evaluated ToF Cameras

In this section, we present a detailed description of some of the most recent ToF cameras released between 2019 and 2020,

TABLE III
SPECIFICATIONS OF MICROSOFT AZURE KINECT AND COMPARISON WITH PREVIOUS RELEASES

Mode	Resolution [px]	FOV [°]	Rate [fps]	Range [m]	t_{exp} [ms]
NFOV unbin.	640 × 576	75 × 65	0, 5, 15, 30	0.5 − 3.86	12.8
NFOV bin.	320 × 288	75 × 65	0, 5, 15, 30	0.5 − 5.46	12.8
WFOV unbin.	1024×1024	120×120	0, 5, 15	0.25−2.21	20.3
WFOV bin.	512 × 512	120×120	0, 5, 15, 30	0.25−2.88	12.8
V1	320 × 240	57 × 43	30	0.4 − 4	auto
V2	512 × 424	70 × 60	30	0.5 − 4.5	auto

TABLE IV
SPECIFICATIONS OF ILLUMINATION SYSTEM FOR THE MICROSOFT AZURE KINECT

Depth Mode	IR Pulses	Pulse Width [μs]	Idle Periods	Idle Time [μs]	Exp. Time [μs]
NFOV unbin. NFOV bin. WFOV bin.	9	125	8	1450	12800
WFOV unbin.	9	125	8	2390	20300

such as the Microsoft Azure Kinect, Helios2, and S100D, together with the L515, which is a solid-state LiDAR. Table II shows a comparison of their main characteristics.

1) Microsoft Azure Kinect: In 2019, Microsoft launched the Microsoft Azure Kinect [56], an AMCW-ToF camera primarily focused on artificial intelligence usage. The Microsoft Azure Kinect also features a color camera, an inertial measurement unit (IMU), and a microphone array. The color camera consists of a high-resolution array of up to 4096 × 3072 pixel. Furthermore, it allows for the generation of color point clouds (PCs), which facilitate the visualization and classification of the observed 3-D scene. The camera supports four different depth sensing modes, depending on the desired FOV and resolution, as presented in Table III. In the binned mode, more stable values of depth and intensity for each pixel, as well as an extended measurement range, are obtained by averaging the values from adjacent pixels. This comes at the cost of reducing the density, i.e., the total number of pixels, of the array. Except for the NFOV-binned mode, the lateral resolution of all the modes outperforms previous releases, such as Microsoft Kinect V1 and V2 [57]. For instance, the resolution may reach up to 1 megapixel for the WFOV-unbinned mode and the measurement range achieves 5.46 m for the NFOV-binned mode. Table IV presents the specifications of the illumination system of the depth camera for the four different modes. The camera adopts a multifrequency approach to increase the depth resolution. The emitted modulated light signal consists of a number of infrared (IR) pulses followed by idle periods which depend on the operative mode.

2) Helios2: In 2018, Sony launched the IMX556PLR DepthSense[1] sensor for AMCW-ToF imaging [55]. The sensor consists of an array of 640 × 480 pixel and combined the SoftKinetic's ToF technology with Sony's backside-illuminated (BSI) technology, yielding an improvement of the light gathering efficiency and a reduction of noise. In 2019, LUCID Vision Labs incorporated it into its Helios ToF camera. Also, other companies such as Basler (Blaze) [58], and Seeed Technology (DepthEye Turbo) [59] built their cameras upon it. In 2020, LUCID Vision Labs announced the next generation of their ToF cameras, the Helios2. This camera supports six different operating models and significantly improves the precision achieved by its precursor, achieving resolutions within the millimeter range. Table V shows the different operating modes of the camera. The Helios2 achieves high accuracy for the distance modes of 5 and 8.3 m by considering a dual-frequency approach of 120+90 MHz with error $\leq \pm 4$ mm$+0.001 \cdot r$, and 90 + 72 MHz with error $\leq \pm 4$ mm $+ 0.002 \cdot r$, respectively, with r being the relative distance between the camera and the observed point. Also, the camera features four vertical-cavity surface-emitting laser (VCSEL) diodes of wavelength $\lambda = 850$ nm.

TABLE V
SPECIFICATIONS OF HELIOS2

Mode	Depth error
1.25 m	± 4 mm
3 m	± 10 mm
4 m	± 10 mm $+ 0.0025 \cdot r$
5 m	± 4 mm $+ 0.001 \cdot r$
6 m	± 10 mm $+ 0.005 \cdot r$
8.3 m	± 4 mm $+ 0.002 \cdot r$

3) S100D: In 2019, Cube Eye Meerecompany released a compact design ToF evaluation board, S100D [60], which features the first Samsung AMCW-ToF sensor, the ISOCELL Vizion 33D. The camera features a sensor array of 640 × 480 pixel for a measurement range from 0.2 m to 4 m and an accuracy of $<\pm 1\% \cdot r$. It is characterized by its low-power consumption of $\leq$1.5 W. The illumination system consists of one VCSEL diode of $\lambda = 940$ nm.

4) L515: In late 2019, Intel RealSense launched a depth camera based on solid-state LiDAR technology, the L515 [38], [61], announced as the world's most power-efficient high-resolution LiDAR camera with power consumption $<$ 3.5 W and weight $<$ 100 g. With a laser emitter of $\lambda = 860$ nm, the camera is suitable for depth streaming preferably for indoor applications, such as warehouse robotics, volumetric measurement, and room scanning, up to 9 m. It enables a pixel array of 1024 × 768 pixel at 30 frames/s due to the low exposure time of $t_{exp} < 100$ ns per depth point and short photon-to-depth latency of 4 ms. Similar to the Microsoft Azure Kinect, it incorporates an IMU and a color camera with a resolution of 2 megapixel. With respect to the depth accuracy, the average depth error and standard deviation at reflectivity $\rho = 95\%$ at 1 m are $<$5 and 2.5 mm, while at 9 m they are $<$14 and $<$15.5 mm, respectively. The specifications of the camera for different modes are described in Table VI.

D. Sources of Error for a ToF Camera

We establish two categories depending on the intrinsic or extrinsic nature of the errors affecting ToF cameras [8], [62].

TABLE VI
SPECIFICATIONS OF L515

Resol. [pix]	Rate[1]	FOV[2][°]	Range[3][m] $\rho = 0.15$	Range[3][m] $\rho = 0.95$
QVGA (320×240)	2.3×10^6	70×55	0.25-3.9	0.25-9
VGA (640 × 480)	9.2×10^6	70×55	0.25-3.9	0.25-9
XGA (1024 × 768)	23.6×10^6	70×55	0.25-2.6	0.25-6.5

[1]The rate is defined as the number of depth points per second.
[2]FOV can vary $\pm 2°$ due to mechanical tolerances.
[3]The maximum range is specified for the center 10% ROI of the image, as long as the operating conditions are fulfilled.

1) *Systematic errors* are derived from the intrinsic properties of the camera and the ToF sensor. Wiggling, pixel-related, amplitude-related, and temperature-related errors belong to this class. Wiggling errors, or circular errors, occur in CW-ToF systems when higher harmonics are present in both, the emitted and reference signals. This leads to a nonlinear, but still monotonic, relationship between depth and phase shift. Wiggling errors were traditionally corrected using calibration data, although alternative correction techniques based on MPI can also be considered [10]. Pixel-related errors are due to the nonuniform charge–voltage conversion, which in complementary metal–oxide–semiconductor (CMOS) technology takes place in parallel in every pixel. This is caused by the variations in transistor and dark currents. This issue, relevant in the early-stage development of CMOS, is currently solved using correlated double sampling (CDS) [63] to remove the undesired voltage offset. In CDS, the output of the sensor is evaluated in two different conditions, one of them known a priori. Both the measurements, one in known conditions and the other in unknown conditions, are required to compose a measurement that relates exclusively (ideally) to the physical property of interest, i.e., depth. Amplitude-related errors may occur because the illumination field decays radially or because of the vignetting effects from the lens. As a result, there may exist nonnegligible light variations between the center and boundaries of the sensor array, which may yield an overestimation of the depth at the external boundaries of the sensor array. Finally, there may exist temperature-related errors. First, the temperature variations in the VCSEL may induce a bias in the phase shift and, also, a quadratic decay of amplitude [64]. Second, the temperature variations within the pixel array will influence the noise of the measurements.
2) *Nonsystematic errors* are caused by ambient conditions, such as signal-to-noise ratio (SNR), MPI, light scattering, and motion artifacts. SNR refers to low signal amplitude compared with the noise floor. It occurs in poorly illuminated areas and highly depends on the depth and amplitude uniformity of the scene. It can be corrected using a low-amplitude filtering and removing corrupted measurements [8], [36]. MPI occurs when, for complex geometries, the modulated light is reflected multiple times across their surface. This results in some pixels receiving the echoes of the optical signals from different paths with the subsequent under- or overestimation of the depth retrieved by such pixels. Light scattering [65] is caused by multiple reflections of incident light between the lens and the sensor and may lead to an underestimation of the depth of distant objects if the light is leaking directly from the source or to an overestimation due to interreflections inside the light system. Motion artifacts [66], [67] are caused by the relative motion between the sensor and the object, which may yield biased depth estimations. Hoegg et al. [68] presented a number of preprocessing techniques for the correction of motion blurring. Also, Lee [66] and Kim et al. [69] presented a correction method for motion blurring by evaluating the relationships between different phase offsets observed at multiple time slots in the ToF sensor.

TABLE VII
SETTINGS OF THE DEPTH MODULE FOR HELIOS2

Variable of control	Default	Min.	Max.
Flying pixel filter	20 mm	0 mm	300 mm
Image accumulation	1	1	32
Confidence threshold	500	0	65535

E. Filtering and Postprocessing Techniques

In this section, we present various tools each camera features to reliably generate a 3-D PC, as well as improving the performance in the presence of noise.

1) The Azure Kinect converts the 2-D depth map taken by a camera into a 3-D PC in the same coordinate system of the camera by performing two consecutive operations (given by the corresponding built-in functions). First, it precomputes a xy-LUT that stores x- and y-scale factors for every image pixel. Then, it determines the pixel's 3-D x- and y-coordinates by multiplying the pixel's z-coordinate with the pixel's x-scale and y-scale factors, respectively.
2) The Helios2 [70] features a flying pixel filter which marks a pixel as invalid when the distance from its surrounding pixels is larger than the user-defined threshold. Helios2 is also capable of accumulating several frames for the depth calculation, which translates into a better noise performance on the resulting data but also on a slower frame rate. The camera provides a confidence value for each pixel, a 16-bit integer obtained by analyzing the variance of the intensity over consecutive frames, which represents a measurement of how reliable the depth data are. In addition, it allows for the configuration of a confidence threshold, i.e., the pixels with values above the confidence threshold are deemed valid. The higher the confidence value for that pixel, the more reliable the depth measurement. Table VII presents the default, minimum, and maximum values for the depth controls of Helios2.
3) Librealsense [71] is an open-source cross-platform to operate RealSense devices, such as L515. As shown in Table VIII, it includes various features in the depth

TABLE VIII
SETTINGS OF THE DEPTH MODULE FOR L515

Variable of control	Default	Min.	Max.
Laser power	100	0	100
Receiver gain	0	9	18
Confidence threshold	1	0	3
Pre-processing sharpening	0	0	5
Post-processing sharpening	1	0	5
Noise filter	3	0	6

TABLE IX
SETTINGS OF THE DEPTH MODULE FOR S100D

Variable of control	Default	Min.	Max.
Flying pixel filter threshold	300	0	4095
Scattering threshold	100	0	4095
Blur multi-freq. threshold	48	0	255
Blur temp. threshold	32	0	255

visualization module, such as the control of the laser power and the receiver gain, a pre- and a postprocessing sharpening, a confidence threshold, and a noise filtering which controls edge and background noise. In addition, it includes a number of postprocessing filters to improve the depth data and minimize noise, such as a decimation filter, an spatial edge-preserving filter [72] to enhance the smoothness of the reconstructed data, a temporal filter which seeks time-domain smoothness, and, finally, a holes' filling filter to generate missing data in the resulting image. The postprocessing tools [71] are included in a separated module and are not considered in this evaluation.

4) The S100D features a flying pixel filter based on a user-defined threshold (the larger the threshold, the wider the range removed), It also permits the user to define a scattering threshold below which the output depth value is set to zero, as well as a motion-blur threshold to avoid aliasing for moving objects which consists of a multifrequency motion blur and a temporal motion blur weight. Finally, it includes a noise reduction filter (a median filter) to remove the spatial noise in the depth frame. The default, minimum, and maximum values considered by the S100D are presented in Table IX.

F. Key Parameters for a ToF Camera

We focus on some key parameters in the performance of any imaging system and, in particular, of ToF cameras.

1) **Warm-up times** are required by the imaging system to reach steady-state conditions and to avoid temperature-related errors due to the thermal fluctuations derived from the heat losses of the electronic components when the camera is initially powered-on. To evaluate this phenomenon, we make use of a 1 × 1 m aluminum panel and coated with barium sulfate ($BaSO_4$), which is almost an ideal Lambertian reflector. The panel is placed at a distance of 1 m with reference to the camera and parallel to the sensor plane. We track the time evolution of the measurements provided by the ToF cameras during 2 h after being powered-on.
2) The **accuracy** stands for the absolute difference between the mean measured and the real values, i.e., ground truth (GT). The precision characterizes the spread of the measurements with respect to the mean measured value and is represented by the standard deviation, σ, of the measurements. This standard deviation depends on the light attenuation and linearly increases with the distance r, i.e., $\sigma \propto r\sqrt{\lambda/\rho\cos\alpha}$, with α being the incident angle, ρ the reflectivity of the target, and λ the wavelength of the light signal [73].
3) The **lateral resolution** is usually bounded by the number of pixels of the sensor, as well as for the quality of the lens which can be characterized by its point spread function (PSF) [74]. If the governing criterion is the number of pixels, the geometry of the pixel and the FOV play a fundamental role. In this work, we make use of the Boehler stars [75] for the evaluation of the lateral resolution of the ToF cameras. As shown in Fig. 3 (center), the Boehler star used in our evaluation has a diameter $m = 20$ cm and consists of 24 alternative sectors. The lateral resolution can be determined as follows:

$$\Delta r_{\text{lat}} = \frac{\pi d M}{n} = \frac{\pi P_1 M}{n P_2} \tag{1}$$

where n is the number of sectors of the star, d is the quotient of the incorrectly measured circle in the middle of the star to the diameter M of the star [18], and P_1 and P_2 represent the number of pixels that each diameter takes in the depth images. If the depth is known, the angular resolution can also be estimated as (2), with z being the depth of the target

$$\Delta r_\theta = \arctan \frac{\Delta r_{\text{lat}}}{z}. \tag{2}$$

4) The **range resolution** is defined as the minimum distinguishable distance which can be determined within the unambiguous range. Based on the voltage resolution, given by the ratio of the total voltage swing and the noise voltage generated by the storage capacitor, the range resolution Δr_r [43] can be expressed as follows:

$$\Delta r_r = \frac{c}{2 f_m} \sqrt{\frac{P_{\text{laser}} + P_{\text{amb}}}{P_{\text{laser}}} \cdot \frac{A}{k_{\text{opt}} q_e \rho \Delta t}} \tag{3}$$

where c is the speed of light, f_m is the modulation frequency, and P_{laser} and P_{amb} are the power of the illumination system and of the ambient light, respectively. In addition, A stands for the total area illuminated, q_e is the quantum efficiency, ρ is the reflectivity of the target, Δt is integration time, and k_{opt} is a constant parameter which defines the optical system. In our experiments, we determine the range resolution as the height difference observed between a test object and the background. As shown in Fig. 3 (left), we make use of three 5 × 5 cm cuboids of heights $h = 3.5$, 7, and 14 mm, respectively.
5) The **edge noise** or **flying pixels** is a particular form of MPI. It occurs when the light beam hits the edge of

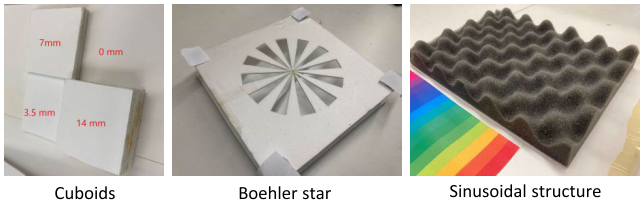

Fig. 3. Test objects used for the experimental evaluation of the ToF cameras.

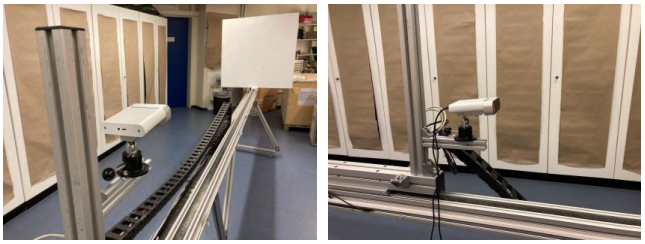

Fig. 4. LTU and experimental setup for warm-up time assessment of the Microsoft Azure Kinect.

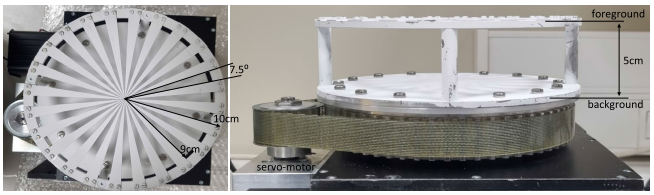

Fig. 5. Experimental setup for the evaluation of dynamic scenes consisting of a rotating Boehler star coupled to a servo motor through a 1:4 reduction system.

Fig. 6. Experimental setup for the assessment of the illumination system using a fast photodetector aligned with the camera.

an object, at which the depth abruptly changes. This may lead to an incorrect estimation of the depth in the incident pixel [76], [77]. To evaluate this phenomenon, we make use of the 1×1 m white panel. We placed the panel at a distance of 1.5 m and assess the PCs generated.

6) The pixels of ToF cameras, as well as of other imaging systems, require a certain amount of time, called exposure or integration time (t_{exp}), to gather sufficient light from the observed scene. A general consideration is that during this time, the position and orientation of the camera and the targets observed in the scene remain invariant. However, as $t_{\text{exp}} \sim \mathcal{O}(10\text{ ms})$, the **relative movement** between the camera and the scene may lead to the observation of light paths for each pixel from different targets during t_{exp} and, therefore, to an erroneous estimation of the depth at the object boundaries, i.e., the appearance of motion artifacts and flying pixels [32]. We evaluate this phenomenon by making use of a turning Boehler star placed at 1 m from the camera and parallel to the sensor plane. We determine the number of pixels whose depth is correctly determined (background and foreground) for various angular rates from 0 to 75 rpm (see Fig. 5 and Section IV-F for more details).
7) The characterization of the **illumination signal** and the resulting optical power are fundamental aspects to achieve a good depth resolution and determine the maximum achievable range of a ToF camera [78] and the range resolution (3).

In addition, we simultaneously evaluate the range and lateral resolutions by making use of a sinusoidal foam structure with amplitude and wavelength equal to 2.5 and 4.5 cm, respectively, as shown in Fig. 3 (right).

IV. Experimental Evaluation

In this section, we present various experiments performed to evaluate the performance of the ToF cameras.[3] As shown in Fig. 4, we make use of a linear translation unit (LTU) with a position accuracy < 1 mm and a bracket which allows for the free rotation of the camera. We remove any possible interference from high-reflectivity objects by covering them with dark cloth and guarantee uniform conditions for all the experiments, as well as minimize the external noise by blocking any external light source. With respect to the evaluation of the effect of the different parameters on the depth estimate, we follow a similar methodology for all the experiments by presenting the average value over 30 acquisitions taken at each depth, from 0.5 to 3 m at intervals of 0.1 m. In addition, we make use of a rotating 20 cm-diameter Boehler star with 48 equi-angular sectors and coated with barium sulfate for the evaluation of dynamic scenes. The Boehler star is coupled to a servo-motor through a 1:4 reduction system, as presented in Fig. 5. Finally, we perform an experimental verification of the illumination system of every camera. We place a high-sensitivity photodetector FPD310-FS-VIS [79] in front of the emitter and parallel to the emitter plane at a relative distance $r_{\text{PD-Camera}} = 0.025$ m. Then, we evaluate the received signal, at the photodetector, as shown in Fig. 6, and present some features such as the width of the train of pulses Δt, the idle periods between them, $\Delta t'$, and the modulation frequencies of the emitted signals. Also, we extract the root mean square (rms) voltage over the pulsewidth, as this is linearly proportional to the emitted optical power. The photodetector is characterized by an active area of 0.13 mm^2, sensitivity to $\lambda \in [400, 1000$ nm], and a bandwidth up to 1.5 GHz.

A. Warm-Up Times

In this test, we evaluate the behavior during the transient period which follows the power-on of the cameras. We select the NFOV-unbinned mode for the Azure Kinect and the $5-$m

[3] A compensation matrix is included in the evaluation of the S100D to mitigate amplitude-related errors observed during calibration [4] as per [5].

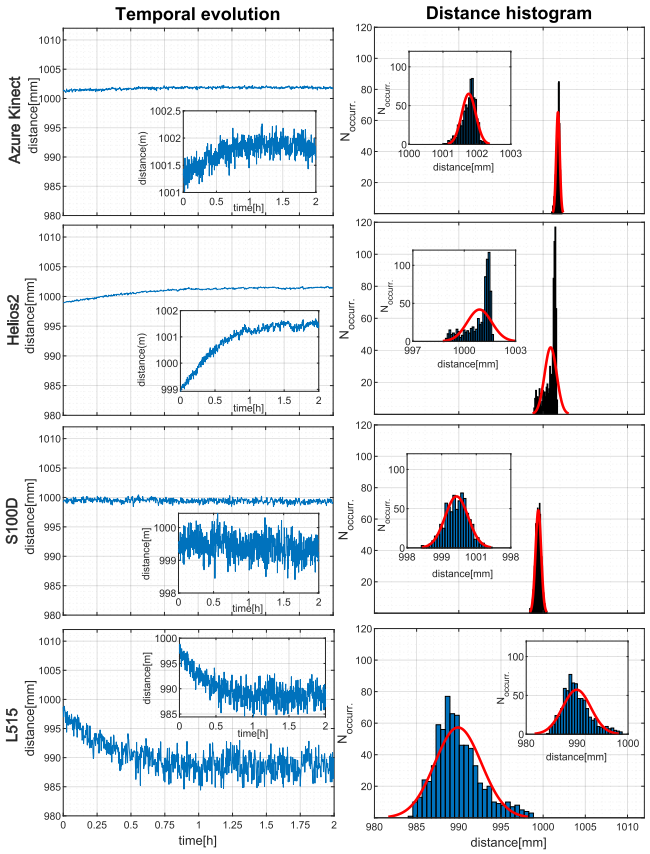

Fig. 7. Warm-up times of the ToF cameras.

distance mode and integration time of 100 μs for the Helios2. All the cameras are powered off for, at least, 2 h before the experiment commences and set to operate in continuous mode. In continuous mode, all the cameras achieve 30 frames/s. We make use of the 1 $\times$ 1 m white panel described in Section III-F at a theoretical distance of 1 m with reference to the camera and parallel to the sensor plane. We store one frame every 10 s during 2 h, yielding 720 frames, and extract the average value of the central area of the sensor array, which comprises 10 pixel at each side of the central pixel, both in the vertical and horizontal directions, as shown in Fig. 7. In addition, we present the histograms of the collected measurements and perform a fit into a Gaussian distribution, since heavy single-side tails are indicative of heavy warm-up effects. We observe that the Azure Kinect reaches steady conditions after 35 min and shows a good fit into the Gaussian curve. The Helios2 requires longer time ($\geq$50 min) to reach steady conditions. This is confirmed by the single-side tail observed in the corresponding histogram. Third, the S100D exhibits a negligible transient period due to its low-power consumption and good dissipation properties [60], which is confirmed by the shape of the distribution observed in its histogram. Finally, the L515 presents the higher initial drift of $\sim$10 mm and requires ($\geq$40 min) to reach steady conditions.

B. Accuracy and Precision

In this experiment, the accuracy and precision of the cameras are evaluated. We calculate the mean and standard deviation over 30 depth frames for each pixel within a 21 $\times$ 21 pixel square region at the center of the sensor array. The average mean absolute error and standard deviations within this region are presented in Fig. 8. We select the WFOV-binned and 5 m modes as representative ones for Microsoft Azure Kinect and Helios2, respectively, as they provide higher accuracy [4]. It is found that the Azure Kinect performs well with error $\leq$ 3 mm for the range considered. Also, we observe that the 5 m mode of Helios2 significantly outperforms the 3 m mode because of the dual-frequency approach adopted, yielding an error $\leq$ 7 mm. The worst accuracy is obtained by the S100D, with an error $\leq$ 10 mm. Also, we obtain error $\leq$ 4 mm for the L515, being specially relevant the excellent performance for shorter distances. We also observe a linear increase in the standard deviation σ with the distance, with σ < 3 mm for all the cameras within the measurement range.

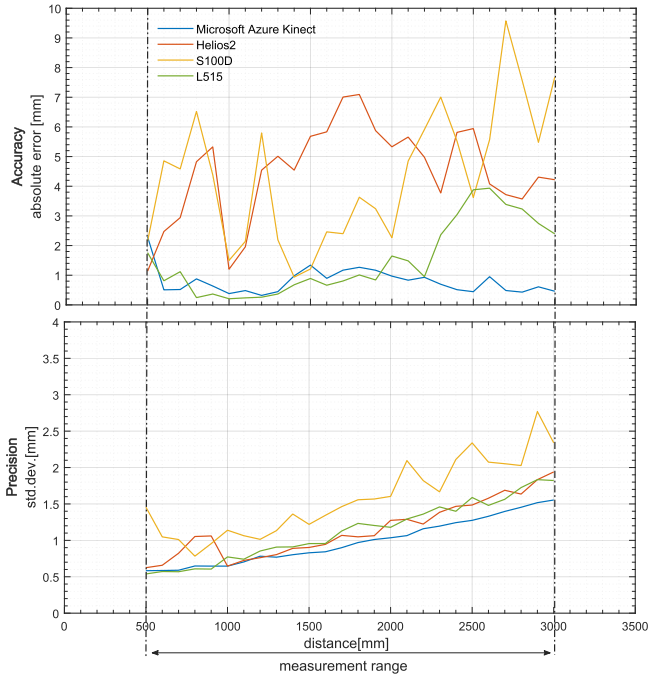

Fig. 8. Accuracy and precision of the ToF cameras.

C. Range Resolution

The range resolution is evaluated by measuring the relative depth of three cuboids with respect to the whiteboard plane on which they are placed, the height of which is taken as zero. As shown in Fig. 3, the heights of the cuboids are $h = 7$ mm (top-left), $h = 3.5$ mm (bottom-left), and $h = 14$ mm (bottom-right). As shown in Figs. 9 and 10, we observe that the cuboids of $h = 7$ and 14 mm are clearly distinguishable for the Helios2 and Azure Kinect and, also, for the S100D after considering the FPN matrix [5]. The cuboid of $h = 3.5$ mm can only be detected by the L515 at $r \leq 1.5$ m, and the lower lateral resolution of this camera at longer distances seriously affects the depth estimation at the edge of the cuboids. In fact, except for Helios2, the relatively low lateral resolution which characterizes the cameras for longer distances yields blurred areas at the transitions between the cuboids, which significantly affects the depth estimation.

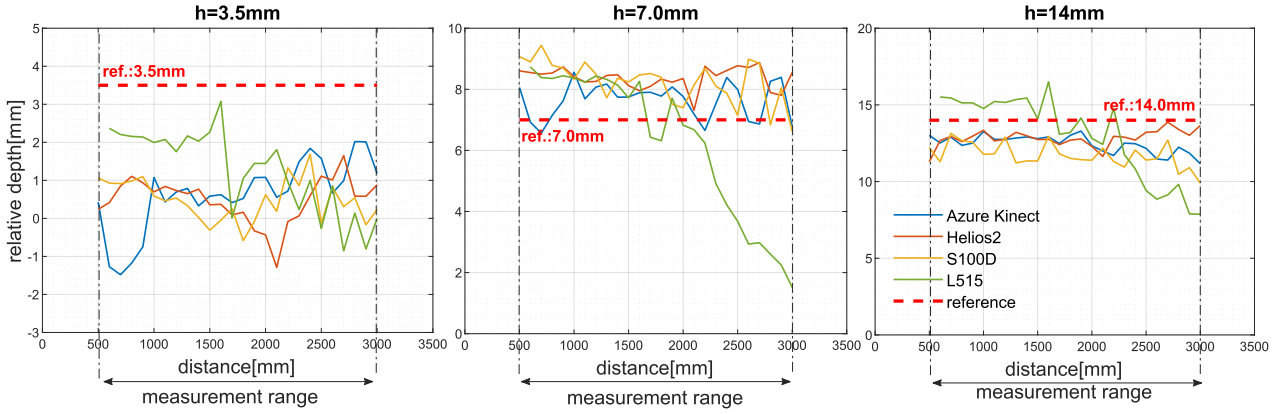

Fig. 9. Measured heights for cuboids at various distances.

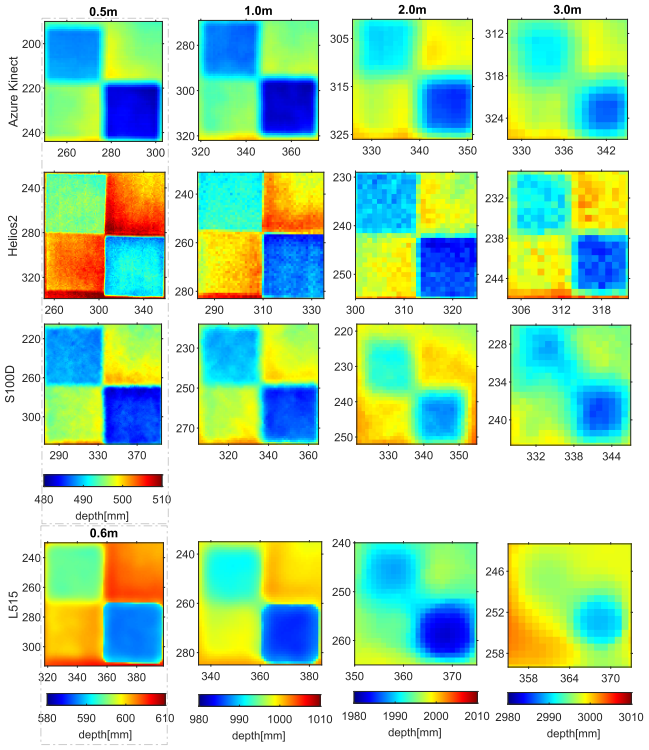

Fig. 10. Depth maps for cuboids of $h = 7$ mm (top-left), $h = 3.5$ mm (bottom-left), and $h = 14$ mm (bottom-right) at various distances $r \in [0.5\text{ m}, 3\text{ m}]$.

TABLE X
THEORETICAL ANGULAR RESOLUTION FOR THE TOF CAMERAS

Camera	Resolution [pix]	FOV [°]	$\Delta r_\theta^{\text{theor}}$ [°]
Azure NFOV unbinned	640 × 576	75 × 65	0.113
Helios2 5 m	640 × 480	69 × 51	0.106
L515	640 × 480	70 × 55	0.115
S100D	640 × 480	60 × 45	0.093

D. Lateral Resolution

First, the theoretical angular resolution, given by the FOV and the number of pixels of the sensor array, is presented in Table X. Then, we make use of the Boehler star described in Section III-F. The Boehler star is characterized by an upper limit for lateral resolution of $\Delta r_{\text{lat}} = 20$ mm. As shown in Figs. 11 and 12, the lateral resolution for all the cameras is $\Delta r_{\text{lat}} \leq 6$ mm for $r \leq 1.4$ m. The outstanding behavior of Helios2 is remarkable, when the multifrequency approach is used, with $\Delta r_{\text{lat}}^{\text{Helios2}} \leq 6$ mm for $r \leq 3.0$ m. Azure Kinect, S100D, and L515 present a similar performance for $r \leq 1.5$ m, from which the performance of L515 progressively deteriorates with respect to the others.

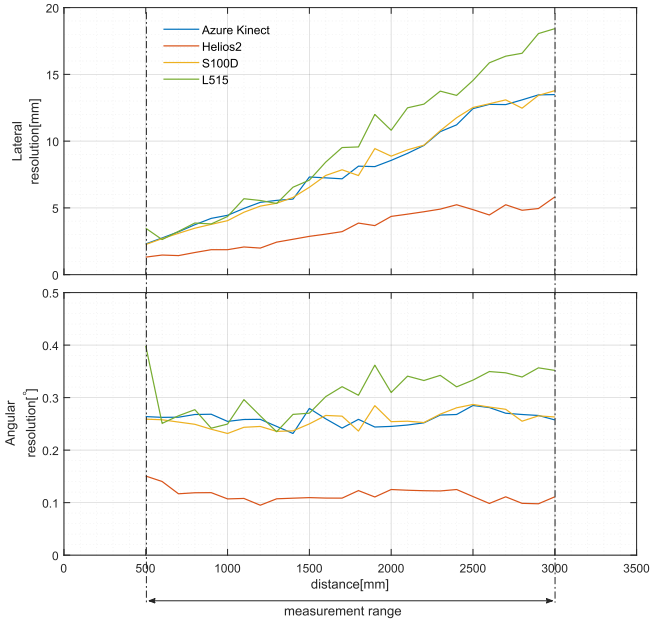

Fig. 11. Lateral and angular resolutions of the ToF cameras.

E. Edge Noise

The possible appearance of the flying pixels at the edges of the 1 × 1 m white panel described in Section III-F is evaluated by representing the PCs generated by every camera at $r = 1.5$ m. The PCs shown in Fig. 13 correspond to five acquisitions, after filtering out the background, registration by means of iterative closest point (ICP) [80], and posterior alignment. We observe that edge noise is specially relevant

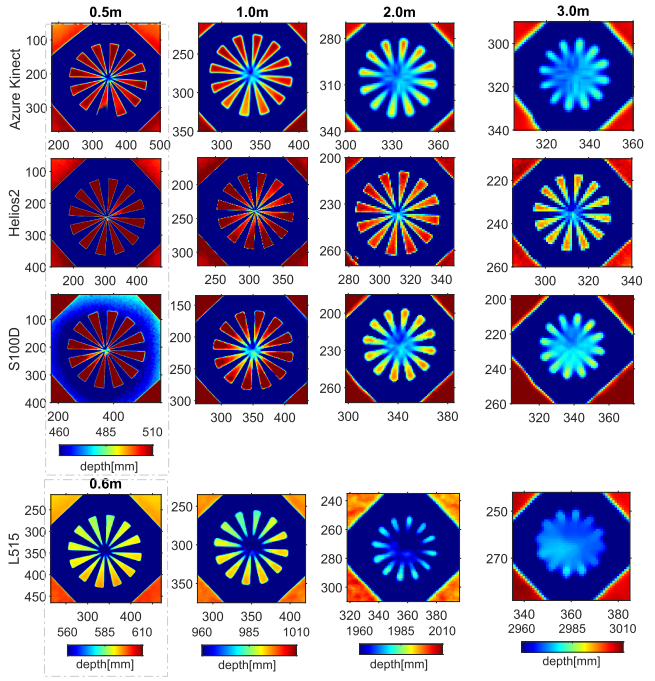

Fig. 12. Depth maps obtained for the Boehler star at various distances.

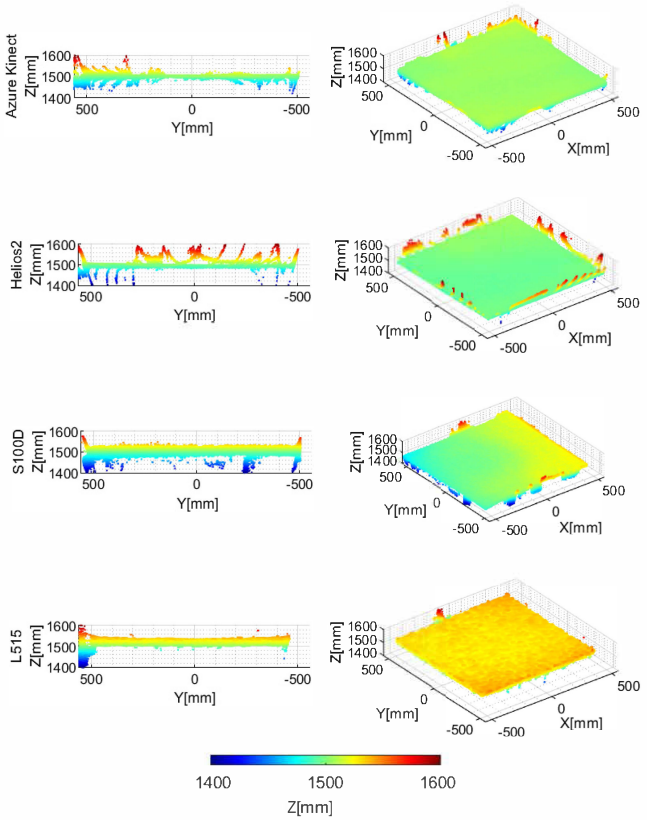

Fig. 13. PCs generated for the 1 × 1 m white panel placed at $r = 1.5$ m.

for S100D and Helios2, affecting most of the perimeter of the target with fluctuations $\Delta z \sim \mathcal{O}(\text{cm})$. In addition, we observe practically no flying pixels on the L515. This is probably because of the microelectromechanical system (MEMS)-based scanning LiDAR operation.

F. Dynamic Scenes

In this experiment, we evaluate the performance of the camera operating under unsteady conditions. We place a turning Boehler star (see Fig. 5 for more details) at 1 m (foreground) from the camera sensor and perpendicular to its optical axis. We attach the Boehler star to a parallel plane (background), at a distance of 5 cm with respect to the foreground plane, which is mechanically bound to a rotating gear at various angular rates[4] from 0 to 75 rpm. Consistently with the rest of the article, we choose the NFOV-unbinned mode for Azure Kinect, 5-m mode for Helios2, and maxrange and VGA resolution for L515. Fig. 14 presents the depth map obtained for one particular acquisition at different angular rates to provide a qualitative description of the lateral and angular resolutions for each of the cameras. We observe that the Azure Kinect does not present significant changes for angular rates $\leq$ 50 rpm, and that the rest shows a progressive deterioration of the angular resolution with the angular velocity. The impact can be specially observed in the S100D at angular velocities $\geq$ 50 rpm. To assess the sensitivity to the incident angle, we manually select a ring with external and internal radii equal to $r_{\text{out}} \approx 8$ cm and $r_{\text{in}} \approx 6$ cm, respectively. This will avoid any impact on the results from the mechanical connection between the Boehler star and the gear. Then we split the ring

[4]The maximum achievable angular rate is limited by current limitations on the control driver to 75 rpm (300 rpm in the servo-motor).

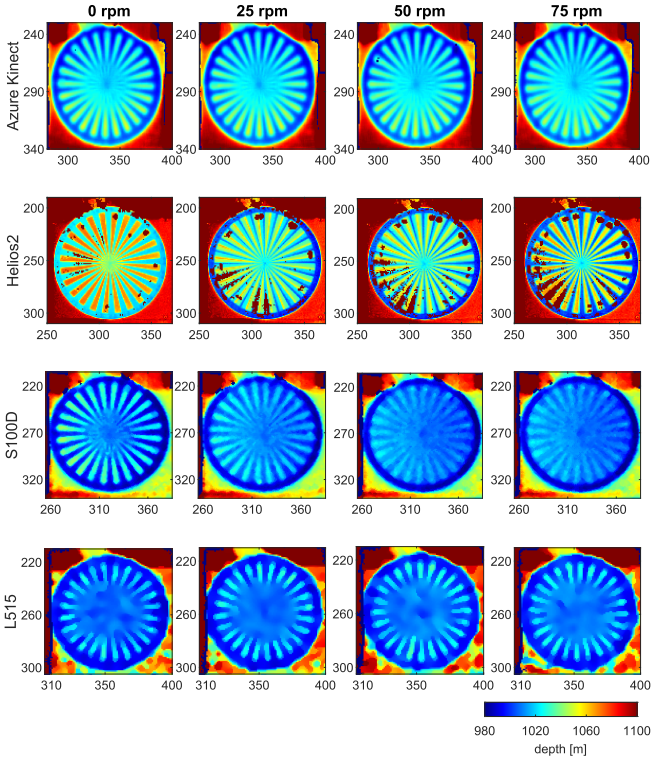

Fig. 14. Depth maps obtained in one single acquisition for the Boehler star at $r = 1$ m for various angular rates.

into four circular segments, as shown in Fig. 15. We present the histograms of the depths retrieved over 30 frames within the area delimited by this ring in Figs. 16–19 by each of the

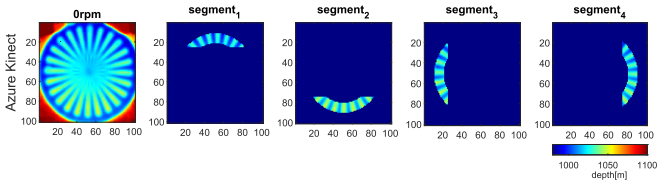

Fig. 15. Segments of the turning Boehler star used for the evaluation of the resolution of the cameras.

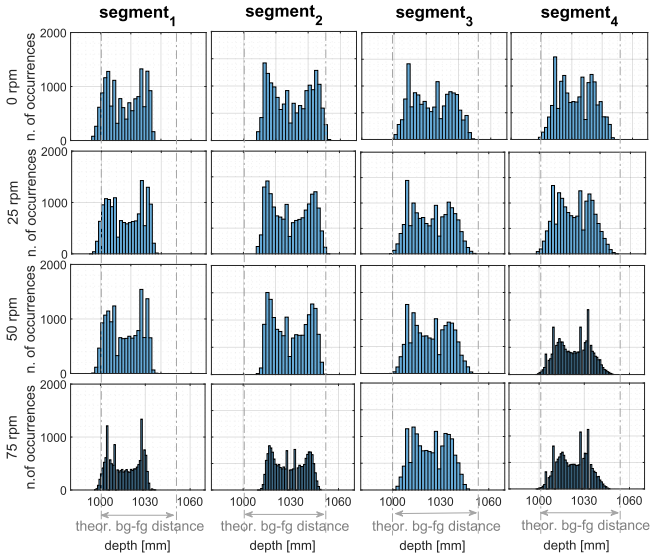

Fig. 16. Histograms of the recovered depths at various angular rates for the Azure Kinect.

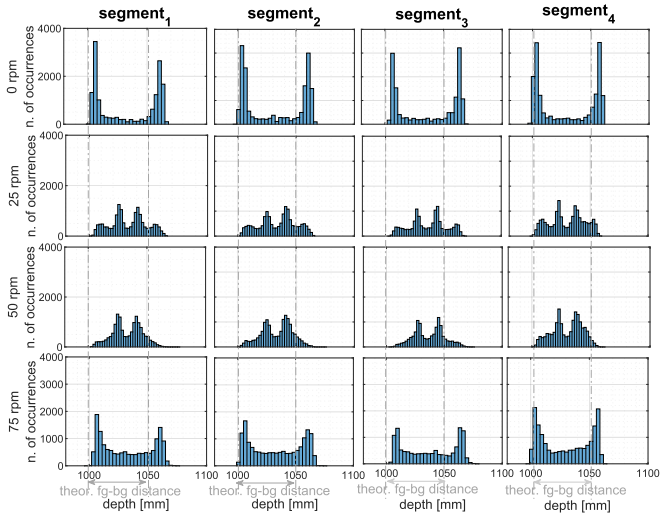

Fig. 17. Histograms of the recovered depths at various angular rates for the Helios2.

cameras for various angular rates $\leq$ 75 rpm. After analyzing the histograms, the following conclusions are drawn.

1) The Azure Kinect shows $\geq$30% of recovered points lying in intermediate distances (flying pixels) between both the planes for all the angular rates and segments. The performance does not suffer significant variations with the angular rate $\leq$ 50 rpm. Also, we observe an underestimation of the distance at which the background

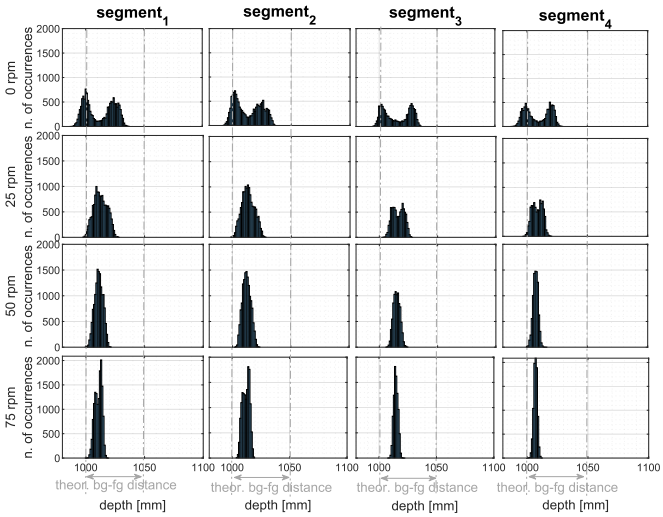

Fig. 18. Histograms of the recovered depths at various angular rates for the S100D.

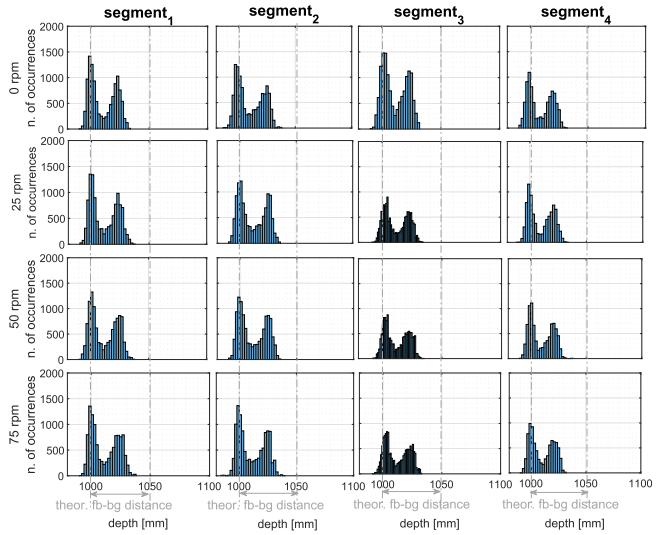

Fig. 19. Histograms of the recovered depths at various angular rates for the L515.

plane is found of $\approx$2 cm, as well as of the distance between both the planes. In addition, we find a better performance in the horizontal segments (segment$_1$ and segment$_2$) with more pronounced peaks in the histograms and fewer flying pixels, especially at low rates.

2) The Helios2 correctly identifies both, background and foreground, planes and presents the best performance for static scenes with only $<$10% flying pixels. However, the performance significantly deteriorates when the target commences to rotate, even at low angular rates. The performance in the horizontal and vertical segments is similar, likely because of the configuration of the illumination system of the camera which consists of four emitters, one at each corner, as shown in Fig. 2.
3) The S100D is the camera with the highest sensitivity to the rotation of the Boehler star. This can be observed in Fig. 14, where there exists a significant reduction of the

lateral resolution when increasing the angular velocity (an increase in the blurry area, especially visible at angular rates $\geq$ 50 rpm). Moreover, Fig. 18 shows the practical disappearance of the peaks corresponding to the locations of the background and foreground planes in the histograms and a complete change in the histogram distribution.

4) The L515 identifies both, foreground and background, planes with two pronounced peaks in the histograms for the four segments. It correctly determines the depth at which the foreground is found, although it underestimates the distance at which the background plane is placed by $\approx$2 cm. We observe that the distribution of background and foreground points is not significantly affected when increasing the angular rate. Although, as we can observe in Fig. 14, the lateral resolution progressively deteriorates when increasing the rotational speed of the Boehler star (see the progressive increase in the blurry area in the central region of the star).

G. Multiple Parameter Evaluation Using Sinusoidal Structure

We make use of the sinusoidal foam structure described in Section III-F to simultaneously evaluate the axial and lateral resolutions, as well as the precision of the cameras. As described in Section III-F, the sinusoidal foam structure has an amplitude and wavelength equal to 2.5 and 4.5 cm, respectively, and is tilted by 0.1 (mm/pixel) (equivalent to $\approx$1.5°) in both the *XZ* and *YZ* planes (see Fig. 26 of Appendix). As shown in Fig. 20, the Azure Kinect can identify the morphology of the target for a larger range, although the accuracy significantly decreases for $r > 2$ m. Helios2 presents a better accuracy for $r = 0.5$ m and 1 m, and acceptable results for $r \leq 2$ m. Finally, S100D and L515 can identify the morphology of the target for $r \leq 1$ m.

H. Characterization of the Illumination System

The received voltage at the photodetector for each of the cameras in terms of rms is presented in Table XI. In addition, we estimate the duration of each train pulse (Δt) and the idle time between consecutive trains ($\Delta t'$). The results for each of the cameras are presented in Figs. 21–25. As a result of our evaluation, the following conclusions may be drawn.

1) The Microsoft Azure Kinect presents one different emitter and set of idle periods and exposure times for narrow and wide FOV modes, respectively (see Table IV). We select the WFOV- and NFOV-unbinned modes as representatives of each of them. Each cycle of the emitted signal consists of nine IR train of pulses with a duration of $\Delta t = 0.125$ ms and idle periods between them of $\Delta t' = 2.39$ ms and $\Delta t' = 1.45$ ms for the WFOV- and NFOV-unbinned modes, respectively. We observe at the photodetector two square-shaped signals of frequencies $f_{\text{High}} \approx 200$ MHz and $f_{\text{Low}} \approx 55$ MHz. We do not observe significant differences between the measured voltages for different frequencies in any of the modes. As expected, we obtain higher voltages for the NFOV-unbinned mode. Figs. 21 and 22 show the received voltages at the photodetector for the NFOV and WFOV modes, respectively.

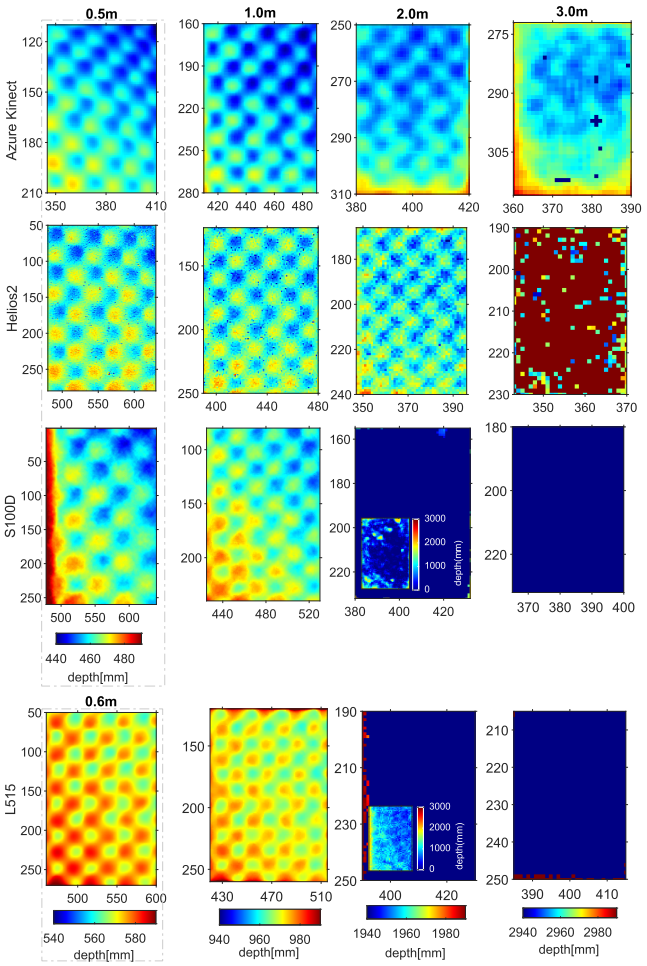

Fig. 20. Depth maps for the sinusoidal foam structure at various distances $r \in$ [0.5 m, 3 m].

TABLE XI
RMS VOLTAGE RECEIVED AT THE PHOTODETECTOR FOR THE TOF CAMERAS

Camera	Mode	Emitter	$V_{f_{\text{High}}}$[V]	$V_{f_{\text{Low}}}$[V]
Azure Kinect	NFOV	-	9.393×10^{-2}	9.414×10^{-2}
	WFOV	-	3.159×10^{-2}	3.161×10^{-2}
Helios2	5 m	Bottom-right	2.655×10^{-2}	2.820×10^{-2}
		Bottom-left	2.879×10^{-2}	2.992×10^{-2}
		Top-right	2.318×10^{-2}	2.414×10^{-2}
		Top-left	2.320×10^{-2}	2.397×10^{-2}
S100D	-	-	1.393×10^{-2}	-
L515	Max. range	-	8.499×10^{-2}	-

2) The illumination system of the Helios2 consists of four emitters (see Fig. 1) and presents six different operational modes. It adopts a dual-frequency approach in two of them, i.e., 5 and 8.3 m distance modes. In this experiment, we evaluate the modulated light signal provided by the four emitters working on the 5 − m distance mode with $f_{\text{High}} = 120$ MHz and $f_{\text{Low}} = 90$ MHz, as it provides the highest accuracy

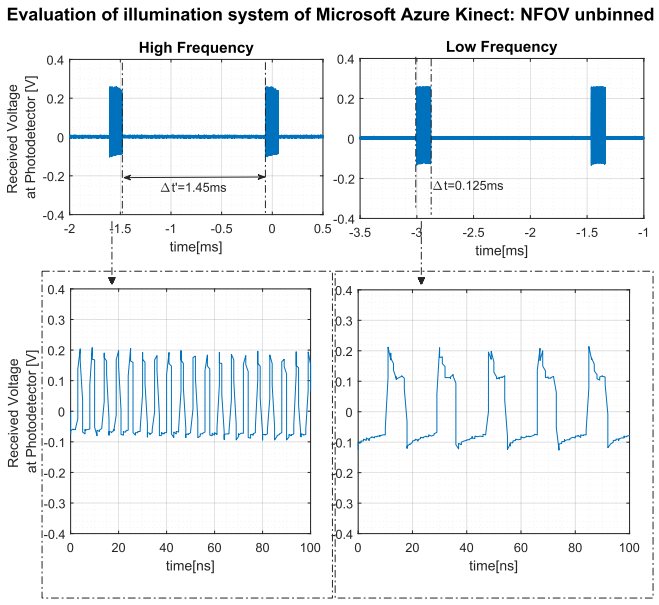

Fig. 21. Received voltage at the photodetector from the optical signal of the Azure Kinect on the NFOV-unbinned mode.

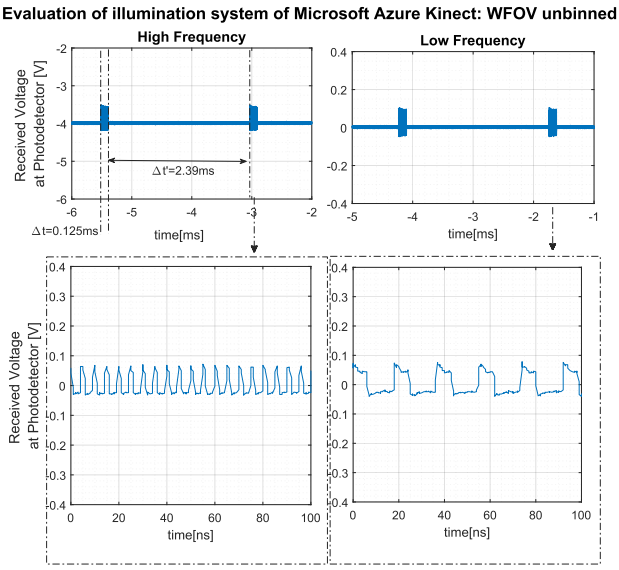

Fig. 22. Received voltage at the photodetector from the optical signal of the Azure Kinect on the WFOV-unbinned mode.

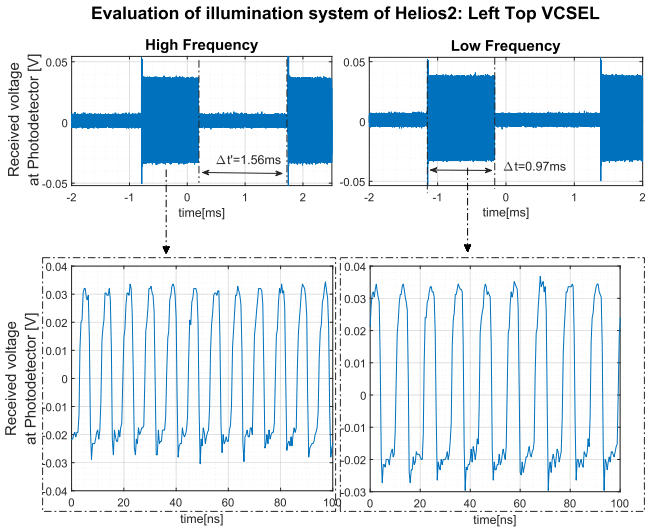

Fig. 23. Received voltage at the photodetector from the optical signal of the Helios2 on the 5-m distance mode (top-left VCSEL).

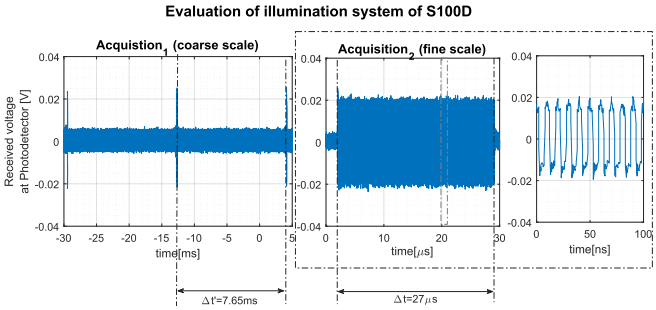

Fig. 24. Received voltage at the photodetector from the optical signal of the S100D.

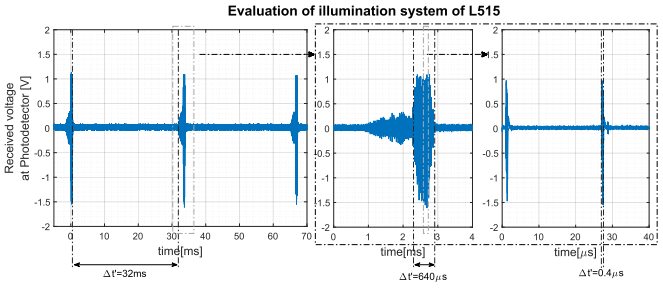

Fig. 25. Received voltage at the photodetector from the optical signal of the L515 on the max range mode.

within our evaluation range. Each train of pulses has a duration of $\Delta t \approx 970$ μs, and there is an idle time between them of $\Delta t' \approx 1.560$ ms. Fig. 23 shows the received voltage at the photodetector for the emitter at the left top corner for the $5-$ m distance mode.

3) The illumination system of the S100D consists of one VCSEL emitter. It is placed at the left side of the camera lens. Fig. 24 shows the received voltage at the photodetector. Since the idle period between acquisitions is quite large, we perform two different acquisitions. The first one considers a coarser scale to evaluate the pulsewidth and idle time, while the second one with a finer scale is used to estimate the rms voltage and the shape of the modulated signal. We observe a train of light pulses of $f = 80$ MHz with a pulsewidth of $\Delta t \approx 27$ μs and idle period between them of $\Delta t' \approx 7.65$ ms.

4) The behavior of the illumination system of the L515, which is a LiDAR, is significantly different. In this case, we evaluate the maxrange operating mode, given by the maximum laser power and the receiver gain. We observe a train of light pulses with a width $\Delta t = 640$ μs and an idle time between them of $\Delta t' = 32$ ms. We observe that the envelop of the light pulse is not constant over

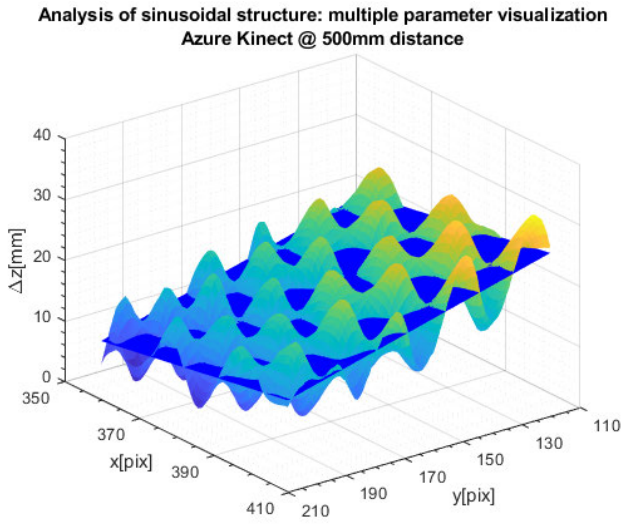

Fig. 26. Measured depth and fit plane by Azure Kinect at 500-mm distance for multiple parameters' visualization.

the pulsewidth and presents an absolute maximum of $|V_{\max}| = 1.61$ Vm and each of the pulses has a duration of $\Delta t_0 \approx 0.4$ μs, as shown in Fig. 21. As this camera is a LiDAR, the nonconstant envelop is due to the fact that only some pulses are directed by the MEMS mirror to our photodetector, which explains the large empty areas in Fig. 25.

V. Conclusion

In this work, we have evaluated the performance of four state-of-the-art depth cameras via various parameters such as the warm-up times, the accuracy and precision, the lateral resolution, and the range (axial) resolution for a measurement range $0.5 \leq r \leq 3.0$ m, as well as the optical power and optical signal. As a result of this evaluation, we have obtained some remarkable results. First, we have observed that the S100D requires much shorter warm-up times than the rest of the cameras ($\Delta t \geq 35$ min). Second, all the cameras show error $\leq$ 10 mm with $\sigma \leq 3$ mm at $r \leq 3$ m. Also, we have observed an outstanding behavior of the Helios2 with respect to the other cameras in terms of lateral (angular) resolution, achieving theoretical maximum lateral resolution for $r = 3$ m. We have found that the L515 performs better for shorter distances in terms of range resolution, being the only one capable of detecting the thinnest cuboid of $h = 3.5$ mm at $r \leq 1$ m, while its performance progressively deteriorates with respect to the others for longer ranges. We have found that the resolution of Helios2 and, specially, of S100D is severely affected in unsteady environments. In addition, we have observed that the edge noise at $r = 1.5$ m is present in all the cameras, although this phenomenon is less acute for the L515. The thorough characterization of the relative performance of this selected group of high-resolution cameras we have provided in this work constitutes a valuable asset for the understanding of their strengths, limitations, and applicability to fields such as autonomous driving and mobile robotics. Prospective research may include the evaluation of the performance for different incident angles, and in the presence of MPI.

Appendix
Orientation of Test Specimen Used for Multiple Parameters' Visualization

Fig. 26 shows the sinusoidal foam used for the visualization of multiple parameters, such as the axial and lateral resolutions, as well as a plane fit to the measured data.

Acknowledgment

The contribution of the first author is part of his Ph.D. thesis conducted at the University of Siegen, Siegen, Germany. The contribution of the second author is part of the master's thesis conducted at the University of Siegen, Siegen, Germany.

References

[1] D. Marr and T. Poggio, "A computational theory of human stereo vision," *Proc. Roy. Soc. London B, Biol. Sci.*, vol. 204, no. 1156, pp. 301–328, 1979.
[2] J. Geng, "Structured-light 3D surface imaging: A tutorial," *Adv. Opt. Photon.*, vol. 3, no. 3, pp. 128–160, Mar. 2011.
[3] R. Schwarte et al., "New electro-optical mixing and correlating sensor: Facilities and applications of the photonic mixer device (PMD)," *Proc. SPIE*, vol. 3100, pp. 245–253, Sep. 1997.
[4] Q. Song, "Performance evaluation of high-resolution time-of-flight cameras," M.S. thesis, Dept. Elect. Eng. Comput. Sci., Siegen Univ., Siegen, Germany, Nov. 2021, doi: 10.5281/zenodo.5665338.
[5] T. Kahlmann, F. Remondino, and H. Ingensand, "Calibration for increased accuracy of the range imaging camera SwissRanger," *Int. Soc. Photogramm. Remote Sens.*, vol. 36, Nov. 2005.
[6] M. Lindner and A. Kolb, "Lateral and depth calibration of PMD-distance sensors," in *Proc. 2nd Int. Conf. Adv. Vis. Comput.* Berlin, Germany: Springer-Verlag, 2006, pp. 524–533, doi: 10.1007/11919629_53.
[7] S. May et al., "Three-dimensional mapping with time-of-flight cameras," *J. Field Robot.*, vol. 26, nos. 11–12, pp. 934–965, Nov. 2009.
[8] S. Foix, G. Alenya, and C. Torras, "Lock-in time-of-flight (ToF) cameras: A survey," *IEEE Sensors J.*, vol. 11, no. 9, pp. 1917–1926, Sep. 2011.
[9] S. Hussmann, F. Knoll, and T. Edeler, "Modulation method including noise model for minimizing the wiggling error of TOF cameras," *IEEE Trans. Instrum. Meas.*, vol. 63, no. 5, pp. 1127–1136, May 2014.
[10] M. Feigin, R. Whyte, A. Bhandari, A. Dorrington, and R. Raskar, "Modeling 'wiggling' as a multi-path interference problem in AMCW ToF imaging," *Opt. Exp.*, vol. 23, no. 15, pp. 19213–19225, 2015.
[11] M. Georgiev, R. Bregovic, and A. Gotchev, "Fixed-pattern noise modeling and removal in time-of-flight sensing," *IEEE Trans. Instrum. Meas.*, vol. 65, no. 4, pp. 808–820, Apr. 2016.
[12] X. Shi, J. Xu, K. Nie, and Z. Gao, "A low kTC noise and low FPN reset method for pixel in ToF image sensor," *IEEE Sensors J.*, vol. 22, no. 3, pp. 2053–2061, Feb. 2022.
[13] Y. He, B. Liang, Y. Zou, J. He, and J. Yang, "Depth errors analysis and correction for time-of-flight (ToF) cameras," *Sensors*, vol. 17, no. 1, p. 92, Jan. 2017.
[14] D. Piatti and F. Rinaudo, "SR-4000 and CamCube3.0 time of flight (ToF) cameras: Tests and comparison," *Remote Sens.*, vol. 4, no. 4, pp. 1069–1089, Apr. 2012.
[15] M. Laukkanen, "Performance evaluation of time-of-flight depth cameras," M.S. thesis, Aalto Univ. School Elect. Eng., Espoo, Finland, 2015. [Online]. Available: http://urn.fi/URN:NBN:fi:aalto-201512165702
[16] S. Pasinetti, M. M. Hassan, J. Eberhardt, M. Lancini, F. Docchio, and G. Sansoni, "Performance analysis of the PMD camboard picoflexx time-of-flight camera for markerless motion capture applications," *IEEE Trans. Instrum. Meas.*, vol. 68, no. 11, pp. 4456–4471, Nov. 2019.
[17] P. Fursattel et al., "A comparative error analysis of current time-of-flight sensors," *IEEE Trans. Comput. Imag.*, vol. 2, no. 1, pp. 27–41, Mar. 2016.
[18] B. Langmann, K. Hartmann, and O. Loffeld, "Depth camera technology comparison and performance evaluation," in *Proc. ICPRAM*, 2012, pp. 438–444.
[19] M. Tölgyessy, M. Dekan, L. Chovanec, and P. Hubinský, "Evaluation of the Azure Kinect and its comparison to Kinect v1 and Kinect v2," *Sensors*, vol. 21, no. 2, p. 413, Jan. 2021.

[20] K. Zhou et al., "Real-time 3D reconstruction of dynamic scenes with multiple Kinect V2 sensors," in *Proc. Int. Broadcast Conv.*, 2021.

[21] J. A. Albert, V. Owolabi, A. Gebel, C. M. Brahms, U. Granacher, and B. Arnrich, "Evaluation of the pose tracking performance of the Azure Kinect and Kinect V2 for gait analysis in comparison with a gold standard: A pilot study," *Sensors*, vol. 20, no. 18, p. 5104, Sep. 2020. [Online]. Available: https://www.mdpi.com/1424-8220/20/18/5104

[22] L. Romeo, R. Marani, M. Malosio, A. G. Perri, and T. D'Orazio, "Performance analysis of body tracking with the Microsoft Azure Kinect," in *Proc. 29th Medit. Conf. Control Autom. (MED)*, Jun. 2021, pp. 572–577.

[23] Q. Wu, "Research on human body detection and tracking algorithm based on Kinect," in *Proc. Int. Conf. Electron. Inf. Technol. Smart Agricult. (ICEITSA)*, Dec. 2021, pp. 7–10.

[24] H. Alaoui, M. T. Moutacalli, and M. Adda, "AI-enabled high-level layer for posture recognition using the Azure Kinect in Unity3D," in *Proc. IEEE 4th Int. Conf. Image Process., Appl. Syst. (IPAS)*, Dec. 2020, pp. 155–161.

[25] F. Wei et al., "Azure Kinect calibration and parameter recommendation in different scenarios," *IEEE Sensors J.*, vol. 22, no. 10, pp. 9733–9742, May 2022.

[26] F. Lourenço and H. Araujo, "Intel RealSense SR305, D415 and l515: Experimental evaluation and comparison of depth estimation," in *Proc. 16th Int. Joint Conf. Comput. Vis., Imag. Comput. Graph. Theory Appl.*, Jan. 2021, pp. 362–369.

[27] M. Servi et al., "Metrological characterization and comparison of d415, d455, L515 RealSense devices in the close range," *Sensors*, vol. 21, no. 22, p. 7770, Nov. 2021. [Online]. Available: https://www.mdpi.com/1424-8220/21/22/7770

[28] S. Giancola, M. Valenti, and R. Sala, *A Survey on 3D Cameras: Metrological Comparison of Time-of-Flight, Structured-Light and Active Stereoscopy Technologies* (SpringerBriefs in Computer Science). Cham, Switzerland: Springer, 2018.

[29] V. Frangez, D. Salido-Monzu, and A. Wieser, "Assessment and improvement of distance measurement accuracy for time-of-flight cameras," *IEEE Trans. Instrum. Meas.*, vol. 71, pp. 1–11, 2022.

[30] S. Tsai, Y. Chang, and T. Sang, "SPAD LiDARs: Modeling and algorithms," in *Proc. 14th IEEE Int. Conf. Solid-State Integr. Circuit Technol. (ICSICT)*, Oct. 2018, pp. 1–4.

[31] A. Kadambi et al., "Coded time of flight cameras: Sparse deconvolution to address multipath interference and recover time profiles," *ACM Trans. Graph.*, vol. 32, no. 6, pp. 1–10, Nov. 2013, doi: 10.1145/2508363.2508428.

[32] H. Sarbolandi, M. Plack, and A. Kolb, "Pulse based time-of-flight range sensing," *Sensors*, vol. 18, no. 6, p. 1679, May 2018. [Online]. Available: https://www.mdpi.com/1424-8220/18/6/1679

[33] A. L. Paredes, M. Heredia Conde, and O. Loffeld, "Effective very-wide-area 3D ToF sensing," in *Proc. IEEE Sensors*, Oct. 2021, pp. 1–4.

[34] S. Mattoccia, *Stereo Vision: Algorithms and Applications*, vol. 22. Bologna, Italy: Univ. Bologna, 2011.

[35] R. Lange, P. Seitz, A. Biber, and R. Schwarte, "Time-of-flight range imaging with a custom solid state image sensor," *Proc. SPIE*, vol. 3823, pp. 180–191, Sep. 1999.

[36] M. Wiedemann, M. Sauer, F. Driewer, and K. Schilling, "Analysis and characterization of the PMD camera for application in mobile robotics," *IFAC Proc. Volumes*, vol. 41, no. 2, pp. 13689–13694, 2008.

[37] R. Horaud, M. Hansard, G. Evangelidis, and C. Ménier, "An overview of depth cameras and range scanners based on time-of-flight technologies," *Mach. Vis. Appl.*, vol. 27, no. 7, pp. 1005–1020, Oct. 2016.

[38] (Aug. 2020). *Optimizing the Intel RealSense LiDAR Camera L515 Range*. [Online]. Available:https://www.intelrealsense.com/optimizing-the-lidar-camera-l515-range/

[39] R. Schwarte, "Dynamic 3D-vision," in *Proc. Int. Symp. Electron Devices Microw. Optoelectronic Appl. (EDMO)*, Nov. 2001, pp. 241–248.

[40] M. Dielacher, M. Flatscher, R. Gabl, R. Gaggl, D. Offenberg, and J. Prima, "Advancements in indirect time of flight image sensors in front side illuminated CMOS," in *Proc. ESSCIRC IEEE 47th Eur. Solid State Circuits Conf. (ESSCIRC)*, Sep. 2021, pp. 139–142.

[41] M. H. Conde, "A material-sensing time-of-flight camera," *IEEE Sensors Lett.*, vol. 4, no. 7, pp. 1–4, Jul. 2020.

[42] Z. Liu and M. H. Conde, "Evaluation and compensation of the effect of dirt on time-of-flight 3D imaging systems," *IEEE Sensors J.*, vol. 22, no. 16, pp. 16595–16606, Aug. 2022.

[43] S. B. Gokturk, H. Yalcin, and C. Bamji, "A time-of-flight depth sensor–system description, issues and solutions," in *Proc. Conf. Comput. Vis. Pattern Recognit. Workshop*, Jun. 2004, p. 35.

[44] O. Gallo, R. Manduchi, and A. Rafii, "Robust curb and ramp detection for safe parking using the Canesta TOF camera," in *Proc. IEEE Comput. Soc. Conf. Comput. Vis. Pattern Recognit. Workshops*, Jun. 2008, pp. 1–8.

[45] S. Acharya, C. Tracey, and A. Rafii, "System design of time-of-flight range camera for car park assist and backup application," in *Proc. IEEE Comput. Soc. Conf. Comput. Vis. Pattern Recognit. Workshops*, Jun. 2008, pp. 1–6.

[46] C. Jing, J. Potgieter, F. Noble, and R. Wang, "A comparison and analysis of RGB-D cameras' depth performance for robotics application," in *Proc. 24th Int. Conf. Mechatronics Mach. Vis. Pract. (M2VIP)*, Nov. 2017, pp. 1–6.

[47] J. Motsch, S. Benammar, and Y. Bergeon, "Interior mapping of a building: A real-life experiment with Microsoft Kinect for windows v1 and RGBD-SLAM," in *Proc. Int. Conf. Mil. Technol. (ICMT)*, May 2017, pp. 728–732.

[48] S. Tang et al., "A vertex-to-edge weighted closed-form method for dense RGB-D indoor SLAM," *IEEE Access*, vol. 7, pp. 32019–32029, 2019.

[49] C. S. Bamji et al., "IMpixel 65nm BSI 320MHz demodulated TOF image sensor with 3 μm global shutter pixels and analog binning," in *IEEE Int. Solid-State Circuits Conf. (ISSCC) Dig. Tech. Papers*, Feb. 2018, pp. 94–96.

[50] P. Seitz, "Smart pixels," in *Proc. Int. Symp. Electron Devices Microw. Optoelectron. Appl. (EDMO)*, Jan. 2001, pp. 229–234.

[51] T. Oggier, B. Buettgen, F. Lustenberger, G. Becker, B. Rüegg, and A. Hodac, "Swissranger SR3000 and first experiences based on miniaturized 3D-ToF cameras," in *Proc. 1st Range Imag. Res. Day ETH Zurich*, 2005.

[52] A. von Beringe, "Performance evaluation of a Range Camera SR400," Institut für Photogrammetrie und Fernerkundung, Technische Universität Wien, Vienna, Austria, 2012. [Online]. Available: https://resolver.obvsg.at/urn:nbn:at:at-ubtuw:1-52321

[53] A. Beringe, "Performance evaluation of a range camera SR4000," Tech. Rep., 2012.

[54] (Sep. 2016). *Softkinetic Introduces Smallest 3D DepthSense Camera Available for Mobile Platforms*. [Online]. Available: https://www.i-micronews.com/softkinetic-introduces-smallest-3d-depthsense-camera

[55] (Jun. 2021). *The Accuracy of Helios2*. [Online]. Available: https://thinklucid.com/product/helios2-time-of-flight-imx556/

[56] (Jun. 2021). *Azure Kinect DK Hardware Specifications*. [Online]. Available: https://docs.microsoft.com/en-us/azure/Kinect-dk/hardware-specification

[57] M. Tölgyessy, M. Dekan, Ľ. Chovanec, and P. Hubinský, "Evaluation of the Azure Kinect and its comparison to Kinect v1 and Kinect v2," *Sensors*, vol. 21, no. 2, p. 413, Jan. 2021.

[58] (Jun. 2021). *Basler Blaze*. [Online]. Available: https://www.baslerweb.com/en/products/cameras/3d-cameras/basler-blaze/

[59] (Jun. 2021). *Seeed Technology DepthEye Turbo*. [Online]. Available: https://www.seeedstudio.com/

[60] (Aug. 2021). *Specification of S100D*. [Online]. Available: http://cube-eye.co.kr/en/#/spec/product_SCUBE.html

[61] (Jan. 2021). *Intel RealSense LiDAR L515 Datasheet*. [Online]. Available: https://dev.intelrealsense.com/docs/lidar-camera-l515-datasheet

[62] M. Lindner and A. Kolb, "Lateral and depth calibration of PMD-distance sensors," in *Advances in Visual Computing*, G. Bebis et al., Eds. Berlin, Germany: Springer, 2006, pp. 524–533.

[63] S. Liu, L. Jiang, H. Yu, Y. Li, D. Ming Xi, and Q. Xie, "A 3-transistor CMOS active pixel with in-pixel correlated double sampling," in *Proc. IEEE Int. Conf. Electron Devices Solid-state Circuits*, Jun. 2013, pp. 1–2.

[64] M. H. Conde, T. Kerstein, B. Buxbaum, and O. Loffeld, "Near-infrared, depth, material: Towards a trimodal time-of-flight camera," *IEEE Sensors J.*, vol. 22, no. 12, pp. 11271–11279, Jun. 2022.

[65] W. Karel, S. Ghuffar, and N. Pfeifer, "Modelling and compensating internal light scattering in time of flight range cameras," *Photogramm. Rec.*, vol. 27, no. 138, pp. 155–174, Jun. 2012.

[66] S. Lee, "Time-of-flight depth camera motion blur detection and deblurring," *IEEE Signal Process. Lett.*, vol. 21, no. 6, pp. 663–666, Jun. 2014.

[67] C. Schockaert, F. Garcia, and B. Mirbach, "Guidance image based method for real-time motion artefact handling on time-of-flight cameras," in *Proc. IEEE Intell. Vehicles Symp. (IV)*, Jun. 2015, pp. 1246–1251.

[68] T. Hoegg, D. Lefloch, and A. Kolb, *Real-Time Motion Artifact Compensation for PMD-ToF Images*. Berlin, Germany: Springer, 2013, pp. 273–288, doi: 10.1007/978-3-642-44964-2_13.

[69] D. Kim et al., "Indirect time-of-flight CMOS image sensor with on-chip background light cancelling and pseudo-four-tap/two-tap hybrid imaging for motion artifact suppression," *IEEE J. Solid-State Circuits*, vol. 55, no. 11, pp. 2849–2865, Nov. 2020.
[70] (Jul. 2019). *Helios Camera Technical Manual*. [Online]. Available: https://thinklucid.com/downloads-hub/#tab-helios-tech-man
[71] (Jun. 2021). *Post-Processing-Filters*. [Online]. Available: https://github.com/IntelRealSense/librealsense/blob/master/doc/post-processing-filters.md
[72] E. S. L. Gastal and M. M. Oliveira, "Domain transform for edge-aware image and video processing," *ACM Trans. Graph.*, vol. 30, no. 4, p. 69, 2011.
[73] D. Anderson, H. Herman, and A. Kelly, "Experimental characterization of commercial flash ladar devices," in *Proc. Int. Conf. Sens. Technol.*, 2005, pp. 1–6.
[74] M. H. Conde, *Compressive Sensing for the Photonic Mixer Device - Fundamentals, Methods and Results*. Cham, Switzerland: Springer, 2017.
[75] A. Orych, "Review of methods for determining the spatial resolution of UAV sensors," *Int. Arch. Photogramm., Remote Sens. Spatial Inf. Sci.*, vol. XL-1/W4, pp. 391–395, Aug. 2015.
[76] I. Chugunov, S.-H. Baek, Q. Fu, W. Heidrich, and F. Heide, "Mask-ToF: Learning microlens masks for flying pixel correction in time-of-flight imaging," in *Proc. IEEE/CVF Conf. Comput. Vis. Pattern Recognit. (CVPR)*, Jun. 2021, pp. 9116–9126.
[77] A. Sabov and J. Krüger, "Identification and correction of flying pixels in range camera data," in *Proc. 24th Spring Conf. Comput. Graph.*, Jan. 2008, pp. 135–142.
[78] R. Lange, "3D time-of-flight distance measurement with custom solid-state image sensors in CMOS/CCD-technology," Ph.D. dissertation, Dept. Elect. Eng. Comput. Sci., Universität Siegen, Siegen, Germany, 2000. [Online]. Available: https://dspace.ub.uni-siegen.de/handle/ubsi/178
[79] (2017). *FPD310 High Sensitivity Fast PIN Photodetector*. [Online]. Available: https://www.menlosystems.com/assets/datasheets/Photodetectors/MENLO_FPD310-D-EN_2022-01-01_3w.pdf
[80] S. Rusinkiewicz and M. Levoy, "Efficient variants of the ICP algorithm," in *Proc. 3rd Int. Conf. 3-D Digit. Imag. Modeling*, May 2001, pp. 145–152.

Alvaro Lopez Paredes (Graduate Student Member, IEEE) received the M.Eng. degree in aerospace engineering from the Technical University of Madrid (UPM), Madrid, Spain, in 2012, and the master's degree in numerical simulation majoring in solid mechanics and the Specialist's degree in numerical simulation majoring in computational fluid dynamics from UPM in collaboration with ANSYS in 2016 and 2020, respectively. He is pursuing the Ph.D. degree in the field of very-wide area 3-D ToF imaging systems by means of adaptive compressive sensing with the Center for Sensor Systems (ZESS), University of Siegen, Siegen, Germany.

In 2020, he joined the Marie Skłodowska-Curie Innovative Training Network Project "MENELAOS^{NT}" at ZESS, University of Siegen.

Qiang Song (Graduate Student Member, IEEE) received the B.Sc. degree from Zhengzhou University, Zhengzhou, China, in 2016, and the M.Sc. degree in communication technology from the University of Siegen, Siegen, Germany, in 2021.

His current research interests include time-of-flight imaging systems and their optimization algorithms for light scattering and multipath interference.

Miguel Heredia Conde (Member, IEEE) received the Dr.Eng. degree in the field of sensor signal processing and the Habilitation degree from the University of Siegen, Siegen, Germany, in 2016 and 2022, respectively.

In 2013, he joined the Center for Sensorsystems (ZESS), University of Siegen. Since then, he has also been a member of the Research Training Group GRK 1564 "Imaging New Modalities." He has been the Leader of the research group "Compressive Sensing for the Photonic Mixer Device" since 2016 and the General Manager of the H2020-MSCA-ITN "MENELAOS^{NT}" since 2020. He is affiliated to the University of Santiago de Compostela (CiTIUS), Santiago, Spain, as a Collaborator. His current research interests include time-of-flight imaging systems, such as those based on the photonic mixer device (PMD), compressive sensing, computational imaging, and unconventional sensing.

Dr. Heredia Conde is a member of ITG/VDE and IEEE/SPS. He was one of the recipients of the 2006 Academic Excellence Prices, awarded by the Government of Galicia, Spain. In 2017, he was awarded the University of Siegen Prize for International Young Academics, for the excellent performance in his doctoral studies.